AIRBORNE LIDAR APPLICATIONS IN FRESHWATER LAKES

by

Michael Robbin Roddewig

A dissertation submitted in partial fulfillment
of the requirements for the degree

of

Doctor of Philosophy

in

Engineering

MONTANA STATE UNIVERSITY
Bozeman, Montana

April 2017

©COPYRIGHT

by

Michael Robbin Roddewig

2017

All Rights Reserved

DEDICATION



2003-2015. Gone but never forgotten, I miss you so much bud.

ACKNOWLEDGEMENTS

There are many people and animals who have helped me along the somewhat convoluted path to getting my doctorate. My apologies to anyone who is forgotten, after over a decade of university my memory is shot!

I need to thank Jenny, my incredible wife, who is more effective than anti-depressants in keeping me sane (the hallmark of a good match, I suppose). Trooper, Yukon, and Storm, my dogs, who have always been there for me, and patiently waited for dinner on late nights when I got too distracted working.

Joe, my advisor, who allowed me the freedom to experiment and eventually land in a field I truly loved.

Jim also deserves thanks for answering all of our silly questions and being patient with us when it was clear we had gotten a bit lost.

My parents deserve some credit as well, especially for their understanding with the variable and somewhat random answer to the question, "when are you going to graduate?"

Finally, the authors wish to acknowledge the support of the Montana Space Grant Consortium. This work was also supported by the Montana Institute on Ecosystems' award from NSF EPSCoR Track-1 under Grant # NSF-IIA-1443108. Any opinions, findings and conclusions or recommendations expressed in this material are those of the author(s) and do not necessarily reflect the views of the National Science Foundation. Additional support was provided by the Montana Research and Economic Development Initiative under Agreement # 51040-MUSRI2015-01 and the National Science Foundation Arctic Observing Network.

TABLE OF CONTENTS

1. INTRODUCTION 1

Objectives 1
Mapping of Invasive Lake Trout 1
Comparison of Measured Lidar Attenuation Coefficient with Modeled Coefficient 4
Detection of Underwater Thermal Vents 4
Prior Work 5
Upcoming Chapters 7

2. LIDAR DESIGN 8

System Design 8
Laser Selection 9
Received Signal and Background Power Modeling 10
Effects of Varying Receiver Aperture Diameter and Field of View 14
SNR and SBR for Lake Trout 17
Coaxial Receivers 19
Tilt Angle 22
Final Optical Design 23
Dynamic Range and Digitizer Considerations 29
Trigger Generation, Computer Interface, and Power Supply 30
Synchronization 31
Operating Software Design 32
Post-Processing Software Design 33
Comparison to the NOAA Fish Lidar 34
Experimental Results 35
Conclusion 37

3. DETECTION AND MAPPING OF INVASIVE LAKE TROUT 40

Introduction 40
Experiments 40
2004 Flight 40
2015-2016 Experiments 42
Discussion 44
Conclusions 48

TABLE OF CONTENTS — CONTINUED

4. LIDAR ATTENUATION 49

Method for Calculating the Attenuation Coefficient from Lidar Data 50
Results for the 2015 and 2016 Flights 51
Wide FOV 51
Narrow FOV 53
Conclusion 57

5. LIDAR DETECTION OF UNDERWATER THERMAL VENTS 66

Discussion and Conclusion 74

6. DISCUSSION OF FRESHWATER AIRBORNE LIDAR AND FUTURE WORK 75

REFERENCES CITED 78

APPENDICES 87

APPENDIX A: Fish Lidar Operation Manual 87

LIST OF TABLES

Table Page

2.1 Lidar parameters to model received signal, SNR, and SBR for various fields of view and receiver aperture sizes. 12

3.1 Fish Hits – 2015 44

3.2 Fish Hits – 2016 45

LIST OF FIGURES

Figure — Page

2.1 Received power (a) and SNR and SBR for a 5-, 10-, and 15-cm-diameter aperture and 5-mrad FOV (parts (b), (c), and (d), respectively). Increasing the aperture diameter provides modest improvements in SNR, although the lidar remains SBR-limited in each case. 15

2.2 Received power (a), and SNR and SBR for a 5-cm-diameter telescope and 10-, 15-, and 20-mrad FOVs (parts (b), (c), and (d), respectively). Increasing the field of view limits the loss from multiply-scattered light. 16

2.3 Received power at 5, 7.5, and 10 meters in depth for (a) 5-15 cm aperture diameter and 5-mrad FOV and (b) 5-20 mrad FOV and 5-cm aperture diameter. 17

2.4 Received power (a) and SNR and SBR plots for a single lake trout, 5-cm-diameter telescope and 5- and 15-mrad FOVs (parts (b) and (c), respectively). 19

2.5 Received power (a) and SNR and SBR plots for 20 lake trout, 5-cm-diameter telescope and 5- and 15-mrad FOVs (parts (b) and (c), respectively). 20

2.6 Received power from 20 lake trout at 5, 7.5, and 10 meters in depth for a 5-cm aperture diameter and a 5-20 mrad FOV. The results are similar to those computed for water (Figure 2.3 on page 17); however, the maximum power at deeper depths is obtained at a FOV of approximately 12.5 mrad. 21

2.7 The probability of the co-polarized receiver at 4 V gain voltage not saturating in five minutes at wind speeds from 1-20 m/s and tilt angles from 5 to 30 degrees. In the final design we chose 15° as our tilt angle. 24

2.8 The layout of the cross-polarized receiver in ZEMAX. The co-polarized receiver is of the same basic design. 26

2.9 A picture of the lidar head, showing the co- and cross-polarized receivers. 27

LIST OF FIGURES — CONTINUED

Figure		Page
2.10	A picture of the lidar head, showing the laser mounted opposite the receivers.	28
2.11	Block diagram of the major electronic components of the lidar system.	31
2.12	The lidar mounted in the plane. The lidar optics are mounted over a hole in the floor of the plane and tilted forward at an angle of 15 degrees to reduce the surface reflection. Behind the lidar head is the electronics case and to the left in the photo is the inverter case.	36
2.13	A representative single lidar shot from Yellowstone Lake in clear water without the presence of fish or a shallow lake bottom. The co-polarized trace is plotted in (a) and the cross-polarized trace in (b). The maximum of the surface pulse appears at approximately 1 meter depth because the surface detection algorithm locates this maximum and then finds the point on the pulse towards the surface where the power is 1% of this maximum, which is the first part of the laser pulse reflected from the surface.	37
2.14	An example single lidar shot from Yellowstone Lake in showing a return typical of fish and a shallow lake bottom. The co-polarized trace is plotted in (a) and the cross-polarized trace in (b). The fish appear as the bump at approximately 2.5 meters highlighted by the red arrow; the lake bottom is just below at approximately 4 meters and appears strongest in the cross-polarized channel.	38
2.15	An image from the cross-polarized channel of the fish return depicted in Figure 2.14 in Yellowstone Lake. The fish are indicated by the red arrow.	39

LIST OF FIGURES — CONTINUED

Figure Page

3.1 On the left is a time-depth profile of airborne lidar from the Southeast Arm of Yellowstone Lake. Depth is shown on the vertical axis, increasing from top to bottom, and time is shown on the horizontal axis, increasing left to right. Strong signals are shown in black, whereas weak or absent signals appear as white. The arrows point to fish hits. The surface of the water appears wavy because it has not been corrected for the motion of the plane. Above the bright surface return is air, which exhibits scattering from snow that was present during the flight. The image is a composite of 500 lidar shots, covering 16.7 seconds or roughly one kilometer of flight. To the right is a close-up image of the fish hits shown to the left. 42

3.2 Map of fish hits from the 2004 flight. Each hit is shown as a green circle. The fish hits in the West Thumb area of the lake were not surprising; however, the hits in the Southeast Arm were at that time previously unknown populations of lake trout but in an area where Park Service models had predicted lake trout would be. In 2007 a National Park Service fisheries boat with gillnets traveled to the location discovered by the lidar and caught many lake trout, a valuable validation of the lidar-generated map. Top of the map points north. Map data © OpenStreetMap contributors. 43

3.3 One of many lake trout caught in 2007 in the Southeast Arm at a site with a large group of fish identified by lidar. Its stomach contains juvenile cutthroat trout. Photograph courtesy Stacey Stigler, National Park Service. 43

LIST OF FIGURES — CONTINUED

Figure Page

3.4 Maps of fish hits identified from the lidar data in Yellowstone Lake from the 2015 and 2016 flights. The flight path taken each year is shown as a black line. 2015 fish hit data is shown in (a), with each hit identified as a red dot. We found several locations in the West Thumb, and the South and Southeast Arms. We did not fly the northeastern section of the lake as lake trout are not expected to be spawning in this part of the lake. 2016 fish hit data is shown in (b), with each location identified as a green dot. For this year we flew the coastline of the entire lake, including all the islands. We saw significantly fewer fish in 2016 than we did in 2015. The most fish activity was again seen in the southeastern arm. Top of the maps point north. Map data © OpenStreetMap contributors. 45

3.5 An example image from the 2015 flight, captured in the Southeast Arm of Yellowstone Lake. The red arrow points to the fish hit, which is the potential spawning site identified at 44.309684° N, 110.25764° W. These fish are immediately adjacent to the edge of an underwater drop-off which some authors have identified as a preferred structure for lake trout spawning sites [1, 2], though not all locations where we identified fish in Yellowstone Lake shared this pattern. 47

4.1 A histogram of the September 28, 2016 attenuation data. The mean was 0.3102 m^{-1}, the median was 0.2603 m^{-1}, and standard deviation was 0.1037 m^{-1}. 52

4.2 The variogram calculated for the September 28, 2016 lidar attenuation data. 54

4.3 A map of the attenuation coefficients from the 2016/09/28 flight. 55

4.4 Histogram of the 2015/09/09 attenuation data. 58

4.5 Histogram of the 2015/09/23 attenuation data. 59

4.6 Histogram of the 2015/10/28 attenuation data. 60

LIST OF FIGURES — CONTINUED

Figure		Page
4.7	Variogram of the 2015 attenuation data.	61
4.8	Map of the 2015/09/09 attenuation data.	62
4.9	Map of the 2015/09/23 attenuation data.	63
4.10	Map of the 2015/10/28 attenuation data.	64
5.1	Lidar image from the (a) co-polarized channel, (b) cross-polarized channel, and (c) depolarization image of a suspected underwater thermal vent in Yellowstone Lake at the West Thumb Geyser Basin. Note that the scales are not equivalent for each channel.	67
5.2	A picture taken from the plane of the thermal vent identified in Figure 5.1. The reddish-brown color could be from iron-oxide, which is common near thermal vents in Yellowstone Lake [3].	68
5.3	A map showing USGS-identified thermal vents and the location of the vent shown in Figure 5.1. The nearest USGS-identified thermal vent is 30 meters away. Top of the maps point north. USGS thermal vent and bathymetry data from [4]. Base map data © OpenStreetMap contributors.	69
5.4	Lidar image from the (a) co-polarized channel, (b) cross-polarized channel, and (c) depolarization image of a second suspected thermal vent. This image shows the same pattern as the first thermal vent from Figure 5.1, but the USGS did not identify any thermal vents near its location.	70
5.5	A picture taken from the plane of the second suspected thermal vent shown in Figure 5.4. The lake bottom is again reddish-brown, which is a common characteristic of thermal vents in Yellowstone Lake.	71

LIST OF FIGURES — CONTINUED

Figure Page

5.6 A map showing USGS-identified thermal vents and the location of the vent shown in Figure 5.4. The nearest USGS-identified thermal vent is over 2 km away. Top of the maps point north. USGS thermal vent and bathymetry data from [4]. Base map data © OpenStreetMap contributors. 72

5.7 An overview map showing the USGS-identified thermal vents in relation to the lidar-identified thermal vents. Top of the map points north. USGS thermal vent and bathymetry data from [4]. Base map data © OpenStreetMap contributors. 73

ABSTRACT

In this dissertation we demonstrate a novel, low-cost, compact airborne lidar designed for marine fisheries research. We discuss the details of our design, show its application to management of invasive lake trout (*Salvelinus namaycush*) in Yellowstone Lake, and mapping of the lidar attenuation coefficient in lake water. Results from 2015 and 2016 are presented, and we also report the lidar detection of underwater thermal vents in Yellowstone Lake.

1

INTRODUCTION

Airborne lidar study of freshwater ecosystems is still a relatively unexplored field, with many applications in improving our understanding of lake ecology. The initial motivation behind designing this lidar was to investigate the potential for airborne lidar to be used to map the spawning locations of invasive lake trout (*Salvelinus namaycush*) in Yellowstone Lake; however, we also discuss mapping of the lidar attenuation coefficient, and the detection of underwater thermal vents.

Objectives

Our major objective was the mapping of invasive lake trout in Yellowstone Lake. We also report the detection of underwater thermal vents in Yellowstone Lake and mapping of lidar attenuation coefficients.

Mapping of Invasive Lake Trout

Yellowstone Lake, Wyoming, USA is the largest body of freshwater above 7000 feet (2100 meters) in North America, and is located entirely within Yellowstone National Park. The lake is home to the largest population of Yellowstone cutthroat trout (*Oncorhynchus clarki bouvieri*) on the continent. Many other species in the park prey on this population of cutthroat trout, including grizzly bears (*Ursus arctos*) and bald eagles (*Haleaeetus leucocephalus*) [5].

In 1994, lake trout (*Salvelinus namaycush*) were discovered feeding on the native cutthroat trout in Yellowstone Lake [6]. One mature lake trout can consume over 40 cutthroat trout per year, and owing to their large size and deep water habitat they are largely immune to predation. These invasive lake trout threaten the existence of

the native cutthroat trout and endanger the entire Yellowstone ecosystem. Efforts to control the lake trout population began the same year. How lake trout were introduced remains the source of some debate, but recent research suggests that they were transplanted from Lewis Lake sometime during the late 1980s [7].

Due to the impact of invasive lake trout, the number of spawning cutthroat trout declined more than 90% between 2000 and 2005. Bear activity at spawning streams experienced a similar decline, as well as catch success by anglers [8], mirroring the decline of Yellowstone cutthroat trout populations.

In the past lake trout fisheries have collapsed due to overexploitation, and thus the Yellowstone Lake population should be susceptible to an intensive removal program [9]. The National Park Service has focused on removing lake trout through passive gill netting. Gill netting begins at the start of the open water season in May and continues through late October. Lake trout spawning typically begins in September, and during the spawning period some gill netting effort is shifted to target these spawning fish [8]. These spawning gill net sets can be highly successful. Gresswell notes that while spawning gill net sets only account for 5% of the Park Service's effort since 2004, they are responsible for 13% of the total annual lake trout catch [10].

However, gill netting large lakes is an expensive proposition. Yellowstone Lake's annual gill netting budget is approximately $300,000, and higher costs have been reported in Idaho [11]. Targeting lake trout spawning areas may then optimize catch success and hasten population decline, while reducing costs [12]. Knowledge of lake trout spawning areas also allows for other experimental population control methods to be applied that target adult lake trout, eggs, and embryos. Because of this, scientific reviews of the lake trout suppression program in 2008 and 2011 emphasized the need

to locate lake trout spawning sites as their population continues to grow and new spawning sites are pioneered [10].

One method of identifying lake trout spawning sites is the use of acoustic 'pingers'. In acoustic tracking, fish are implanted with acoustic transmitters and then acoustic receivers are placed at strategic locations underwater to follow the movements of the tagged fish. The method is accurate and can allow the habits of individual fish to be tracked over a long period of time, but requires invasive surgery to implant the acoustic transmitters in the fish and then time to place and periodically download data from the acoustic receivers. The coverage of the receivers is also limited to approximately 500 meters, and data must be returned to the manufacturer for processing before examination.

Airborne lidar presents an alternative method for locating lake trout spawning sites. Airborne lidar can be used to identify congregations of fish, and thus can be used to identify spawning sites in a manner similar to that done with acoustic tracking [10, 13]. Over the past several decades, airborne lidar has become an established technique to detect and profile fish in the open ocean [14–19]. The data produced is similar to what would be obtained from a traditional acoustic echosounder [20, 21]. With calibrated laboratory measurements of the reflectivity of fish species of interest, accurate estimates of biomass can be made from lidar data [20,22,23]. Using airborne lidar for fisheries surveys allows larger areas to be rapidly mapped and at vastly lower cost than with a surface vessel [18]. A typical flight of Yellowstone Lake takes approximately two hours, covers over 160 km, and costs only $2000. Data are often available within 24 hours of the flight. While airborne lidar is has been demonstrated in the ocean for fisheries surveys, the technique has not been well studied in lakes.

Comparison of Measured Lidar Attenuation Coefficient with Modeled Coefficient

The lidar attenuation coefficient α varies between the beam attenuation coefficient c and the diffuse attenuation coefficient of downwelling radiance K_d [19, 24, 25]. In [26] we used a model from [27] to derive optical properties for modeling the lidar performance in Yellowstone Lake. However, it is not known how accurate this model was. Numerous parameters had to be assumed from other, similar, lakes, including the colored dissolved organic matter (CDOM, referred to as "yellow substance" by Gallie) concentration and the suspended mineral concentration. This is problematic; Kirk notes that estimates for the absorption coefficient of CDOM vary widely, even for lakes in the same general area [28].

In the paper, penetration depth was used as a crude measure of model fit. Here, we compare the modeled lidar attenuation coefficient with actual measurements of the lidar attenuation coefficient taken from Yellowstone Lake.

Detection of Underwater Thermal Vents

Yellowstone is famous for its numerous geysers, hot springs, and other thermal features. While these features have been known of and studied since the 1800s, the existence of thermal activity in Yellowstone Lake was not realized until the 1980s [29]. Several studies have been performed since then, utilizing SCUBA divers, remotely-operated vehicles (ROVs), and high-resolution sonar [30–33]. Detection of underwater thermal vents with airborne lidar has not been previously reported.

Remsen and Morgan ([29] and [33], respectively) both report that many underwater vents emit bubbles of steam and CO_2 and often exist in domal structures where the sediments have been forced upward by the gas or created by sediments entrained in the gas bubbles. These domes may rise to several meters in height [33]. The warmer water and various chemicals emitted by these vents are a significant

influence on the geochemical composition of Yellowstone Lake and the flora and fauna [34].

The underwater fumaroles and vents are often surrounded by diverse communities of bacteria, plants, and animals that would not normally exist in a cold, oligotrophic lake [29, 35]. One vent in particular in the West Thumb Geyser Basin was dubbed "Cutthroat Jacuzzi" because of the cutthroat trout that school to feed on the numerous zooplankton that live in its warm waters [32].

In Chapter 5 we discuss the use of airborne lidar to detect underwater thermal vents.

Prior Work

Murphree et al. were the first to introduce the idea of using an airborne lidar to detect fish in 1974 [14]. They introduced a mathematical model for detection of fish schools in the ocean. Their model looked simply at power density beneath the ocean as a function of surface roughness and depth and then computed the power received back at the detector. They concluded that the reflected power is of sufficient magnitude to locate fish schools.

Squire et al. were the first to report successfully detecting fish schools using a Navy lidar in 1981 [15]. They developed an airborne laser radar as part of the Optical Ranging, I.F.F., and Communications (ORIC) program, whose main goal was to investigate the feasibility of underwater target detection with a pulsed laser system. In two experiments, one at Key West and the other off the coast of New Jersey, they were able to demonstrate lidar detection of fish schools but did not attempt visual or other confirmation of their findings.

Gordon described a Monte Carlo model of oceanic lidar that included the effects of multiple scattering in 1982 [24]. His work forms the basis of the equation we use to model the attenuation of the lidar beam in lake water.

Hoge et al. first described the detection of subsurface scattering layers using a NASA 532 nm lidar off the coast of Virginia in 1988 [36]. They mapped a subsurface oceanic plume that extended for several kilometers, but did not attempt further investigation to determine what this plume was. Bukin described the detection of subsurface scattering layers in 1998 [37] and Vasilkov later reported the detection of subsurface scattering layers using polarized lidar in 2001, investigating the potential for lidar to profile chlorophyll concentrations [38].

The use of lidar for bathymetry has been extensively investigated by Guenther. In 1985 he published a technical report describing the design of a lidar system for bathymetry and detailed some of the technical problems encountered when trying to achieve high accuracy [39]. In 1986 he published a second report discussing the effects of wind and tilt angle on the surface return from airborne lidar [40]. In 1996 he published a report discussing the advances in lidar design for bathymetry, describing the SHOALS system he developed for NOAA [41].

Churnside has been actively working on investigating the applications of airborne lidar in the ocean. In 1991 he measured the optical properties of several Pacific fish [22] and then reported lidar profiles of fish schools in 1997 [23] and 2001 [18]. He has also compared echosounder and lidar measurements of fish schools and scattering layers [20, 21, 42], measured the lidar attenuation coefficient [25], described the lidar detection of internal waves and bubbles [43–45], and the lidar detection of scattering layers [46]. Most recently he published a paper reviewing the applications of airborne marine lidar [19].

All of these studies have focused exclusively on the ocean. Gauldie discussed the possibilities for lidar to revolutionize the monitoring of fisheries in [17], and was the first to present the idea of using lidar in freshwater ecosystems. Shaw and Churnside were the first to attempt the use of lidar in a freshwater lake. They flew the NOAA Fish Lidar over Yellowstone Lake in an attempt to locate the spawning sites of invasive lake trout in 2004 [47]. This study was successful, but no further investigation was performed.

Upcoming Chapters

The remainder of the dissertation proceeds with a discussion of the design of the lidar in Chapter 2, results from the the lake trout surveys in Chapter 3, a comparison of the measured and simulated lidar attenuation in Chapter 4, and a report on lidar detection of underwater thermal vents in Chapter 5. Chapterchp:conclusion concludes the dissertation and discusses future work.

8

LIDAR DESIGN

In this chapter we discuss the design decisions we made when building our lidar, including the optical, hardware, and software components. The initial requirements were that the lidar be capable of dual-polarization measurements, easily transportable and small enough to fit in a single-engined plane, and robust. Our goal was to create a lidar that would able to study multiple species and limnological parameters. Cost was also a significant factor, and we used many components that were already available in our laboratory. The software used primarily open-source libraries and languages. This chapter draws largely from [26].

System Design

Cost was a driving design requirement and shaped many of the design decisions we made. This lidar was intended to cost under $100,000 USD and be flown in small, single-engine aircraft, such as the Cessna 185, to minimize operating costs. Penetration to large depths was not a requirement because during the spawning season lake trout are at depths of just a few meters [12,48], and data from local lakes indicated plankton rarely existed in great numbers beyond 15 meters [49].

A major feature of this lidar was the ability to make measurements of both the co- and cross-polarized signals, and thus measure the depolarization ratio. Fish, zooplankton, and phytoplankton all depolarize lidar signals to varying extents, and measuring the amount of depolarization can provide useful information [19].

In the following sections we discuss some of the design decisions we made for various parts of the lidar system. The first sections discuss the optical design, covering choice of laser, field of view, and aperture size, and then moving onto coaxial vs. separate receivers for each polarization, and the lidar tilt angle. We then cover the

more interesting aspects of the electronics and software design, and conclude with example data and a comparison with the NOAA Fish Lidar, which performs similar work in the ocean.

Laser Selection

Important considerations for laser selection are the wavelength, divergence, and the pulse length and repetition frequency. 532 nm is the most common wavelength for marine lidar, owing to the wide availability of rugged, small, and inexpensive lasers, and favorable absorption characteristics in natural waters. While the absorption of light in pure water has a minimum at approximately 420 nm [50] the absorption minimum shifts to longer wavelengths as the concentration of dissolved organic matter increases [19,51]. Morel developed a model that related the chlorophyll concentration to the attenuation coefficient of downwelling irradiance, K_d, which showed that at chlorophyll concentrations above approximately 0.2 mg/m^3 the attenuation at 500 nm is less than that at 400 nm [52]. Chlorophyll-a concentrations are well above this level in Flathead Lake [53] and Yellowstone Lake [54], especially during the summer months. For these reasons we chose 532 nm as our design wavelength.

The laser pulse width creates a limit on the accuracy of depth information that can be obtained by the lidar. For the fisheries application we simply need to detect the presence of fish and possibly quantify the biomass of the fish present in a given area [42]. We are not able to distinguish fish species; suspected lake trout spawning sites are identified by consideration of the location and depth of the detected fish in concert with other ecological parameters in a manner similar to what is used with acoustical tracking devices [10,13]. In this case, the loss of precision due to the laser pulse width is not an impediment. When profiling plankton layers, precise measurements of depth

are more useful, but these measurements can be easily obtained from a surface vessel. Thus, while short pulse width was important, it was not a major requirement.

The pulse repetition frequency (PRF) limits the maximum speed that the aircraft can travel while maintaining overlap between adjacent shots and must be high enough to allow for a reasonable flight speed if continuous coverage along the flight path is desired. Thought must also be given to the laser divergence, as it is desirable to match the divergence and the field of view of the receiver. Broadening a narrow laser beam is often easily accomplished with a negative lens.

Based on previous positive experiences with Big Sky Laser (now known as Quantel USA), we chose the air-cooled, diode-pumped, 40-mJ Centurion laser (Quantel USA, Bozeman, MT). This laser is similarly robust to lasers we have used in the past and is diode-pumped, which provides better electrical efficiency. The Centurion outputs a 40-mJ pulse at 1064 nm, which is doubled to 532 nm. Any residual energy at 1064 nm is blocked. Pulse energy at 532 nm is 26 mJ, output divergence is 5 mrad, pulse length is 7.2 ns, and maximum pulse repetition frequency (PRF) is 100 Hz. Our pulse-limited depth resolution is 80 centimeters in water, and with an 800 MSPS digitizer the sample-rate-limited depth resolution in water is 14 centimeters.

Received Signal and Background Power Modeling

Field of view (FOV) and receiver aperture size are crucial considerations, as the product of aperture area and field-of-view projected solid angle gives the radiometric throughput for an optical receiver [55]. A wide field of view will reduce the effective attenuation in water by capturing multiply-scattered photons, but will increase the amount of unwanted background light received. To help choose these parameters we

modeled the signal-to-noise ratio (SNR) and signal-to-background ratio (SBR) for various FOV and receiver aperture sizes.

The received electrical lidar signal power $P_{\text{electrical}}(z)$ in watts at depth z is calculated similarly to Churnside [19].

$$P_{\text{electrical}}(z) = \left(\frac{E_0 A T_S^2 \eta n v}{2(nH+z)^2} \beta(\pi, z) e^{-2\alpha z} \right)^2 R_L, \tag{2.1}$$

where E_0 is the laser pulse energy, A is the receiver aperture area, T_S is the surface transmission, η is the photomultiplier tube (PMT) responsivity, n is the water index of refraction, v is the speed of light in vacuum, H is the plane altitude, $\beta(\pi, z)$ is the volume scattering coefficient and is assumed to be constant over depth, α is the lidar attenuation coefficient and is discussed below, and other parameters are given in Table 2.1. The laser divergence and receiver FOV are assumed to be matched and in full overlap, and for this simple model we ignored the effect of polarization and the transmission of the optics. For our lidar we used a photomultiplier tube (PMT) receiver, which directly drives the digitizer.

The water surface is assumed to be flat and the reflection at the surface is computed using the Fresnel equations for the lidar tilt angle. The value obtained for the surface transmission of $T_S = 0.951$ for this simple model does not differ significantly from a rigorous computation by Mobley for a polarized sky and various wind speeds [57].

The lidar attenuation coefficient α is an "effective" attenuation coefficient, which accounts for the effects of multiple scattering in the water. The following equation is from Churnside [19], which was derived from Monte Carlo simulations of oceanic lidar by Gordon [24].

$$\alpha = K_d + (c - K_d) e^{-0.85cD}, \tag{2.2}$$

Table 2.1: Lidar parameters to model received signal, SNR, and SBR for various fields of view and receiver aperture sizes. Laser parameters are from the Quantel Centurion laser. Digitizer parameters are for the GaGe CS148001U USB Digitizer. Photomultiplier tube (PMT) parameters are for the Hamamatsu H7680. Parameters not used in the simulation are unlisted.

Laser	Wavelength	532 nm
	Pulse Width τ_p	7.2 ns
	Pulse Energy E_0	26 mJ
Digitizer	Voltage Step Size δ_V	134 μV
	Bandwidth B	700 MHz
PMT	Anode Responsivity η (at 2.5 V gain voltage)	440 A/W
	Dark Current I_D	200 nA
Other	Load Resistance R_L	50 Ω
	Lidar Tilt Angle	15°
	Filter Bandwidth B_f	2 nm
	Water Index of Refraction n	1.333
	Altitude H	300 m
	Single-Scatter Albedo [56]	0.85

where D is the lidar spot diameter on the water surface, c is the beam attenuation coefficient, and K_d is the diffuse attenuation coefficient. This effective attenuation coefficient accounts for the field-of-view loss that results from scattering in the water [39, 58].

By definition, $c = a + b$ where a is the attenuation coefficient and b is the scattering coefficient. Measurements of optical properties of local lakes are lacking, so for simulation we were forced to estimate these parameters. Models from Gallie [27] were used to estimate a and b given chlorophyll-a concentration, suspended mineral concentration, and colored dissolved organic matter (CDOM, referred to as "yellow substance" by Gallie). The chlorophyll-a concentration of 0.75 μg/L is a representative number from Yellowstone Lake [54], while the suspended mineral concentration of 3 mg/L, and CDOM value of 0.3 m^{-1} (at 350 nm) are numbers from

Chilko Lake [27], an oligotrophic lake in British Columbia similar to Yellowstone Lake, as these data were unavailable for local lakes. These values yielded $a = 0.179$ m^{-1} and $b = 0.8427$ m^{-1} at 540 nm. Thus, for simulation the beam attenuation coefficient $c = 1.0214$ m^{-1}.

To compute the diffuse attenuation coefficient we used the equation from Lee [59],

$$K_d = a + 4.18 b_b \cdot \left[1 + 0.52 e^{-10.8a}\right], \tag{2.3}$$

where b_b is the backscattering coefficient. To calculate b_b we integrated the phase scattering function values listed in Mobley [60] with the calculated total scattering coefficient b from above to yield $b_b = 0.0153$ m^{-1}. Thus, $K_d = 0.2474$ m^{-1}. This result was verified using a different expression from Kirk that yielded an estimate for K_d of 0.2655 m^{-1} [61].

To determine the volume scattering coefficient $\beta(\pi;\lambda)$ we used the definition of the spectral volume scattering phase function $\tilde{\beta}(\phi;\lambda)$, where $\tilde{\beta}(\phi;\lambda) \cdot b(\lambda) = \beta(\phi;\lambda)$. The value of the phase scattering function was again taken from Mobley [60], $\tilde{\beta}(\pi;\ 530\text{ nm}) = 3.154 \cdot 10^{-3}$ sr^{-1}, which yields $\beta(\pi;\ \sim 532\text{ nm}) = 3.9 \cdot 10^{-3}$ m^{-1}sr^{-1}.

In computing the SNR we took into account shot and ideal quantization noise. Shot noise power is defined as $P_{\text{shot noise}} = 2qIBR_L$, where q is the elementary charge, I is the output current of the PMT (including the background signal and dark current), B is the system bandwidth, and R_L is the load resistance [62]. The quantization noise power is defined as $P_{\text{quantization noise}} = \delta_V^2/12$ where δ_V is the digitizer voltage step size. Thus, SNR is computed as (expressed in decibels)

$$\text{SNR}_{\text{dB}} = 10 \cdot \log_{10}\left(\frac{P_{\text{electrical}}}{P_{\text{shot noise}} + P_{\text{quantization noise}}}\right), \tag{2.4}$$

and SBR is computed as (in decibels),

$$\mathrm{SBR_{dB}} = 10 \cdot \log_{10}\left(\frac{P_{\text{electrical}}}{P_{\text{background}} + P_{\text{dark current}}}\right), \tag{2.5}$$

where $P_{\text{dark current}} = I_D^2 R_L$. $P_{\text{background}} = L_B A \Omega_{\text{FOV}} B_f$, where Ω_{FOV} is the receiver field of view solid angle and B_f is the filter bandwidth given in Table 2.1. L_B is the background radiance, which was computed to be 100 $\mathrm{mWm^{-2}sr^{-1}nm}$ using MODTRAN (MODerate resolution atmospheric TRANsmission) for a standard rural atmosphere with 5-km visibility at Yellowstone Lake.

Effects of Varying Receiver Aperture Diameter and Field of View

To determine an optimal receiver configuration, we modeled the effects of varying the receiver aperture diameter and field of view. We first tested aperture diameters from 5 to 15 cm for a 5-mrad FOV, which matches the unexpanded laser beam divergence. The results are shown in Figure 2.1. Increasing receiver aperture size improves the signal to noise ratio (by increasing the received signal power), although because of our high background radiance the lidar remains SBR-limited in all configurations. If the background light were to be lessened, the simulation indicates that for a 5-mrad field of view a 15-cm-diameter telescope would be optimal, with maximum depth of penetration at 13 meters; however, the gains to be had by increasing aperture diameter are quite modest, especially given the expense of a larger aperture and the difficulty of fitting a large telescope in a small airplane. The results for a 15-mrad FOV are similar to those for the 5-mrad FOV.

The same plots were generated for 10-, 15-, and 20-mrad fields of view for a 5-cm-diameter aperture (shown in Figure 2.2) and follow the same pattern as increasing the aperture size, but with slightly larger improvements in penetration depth compared to the aperture diameter case. Each configuration was again SBR-limited, although

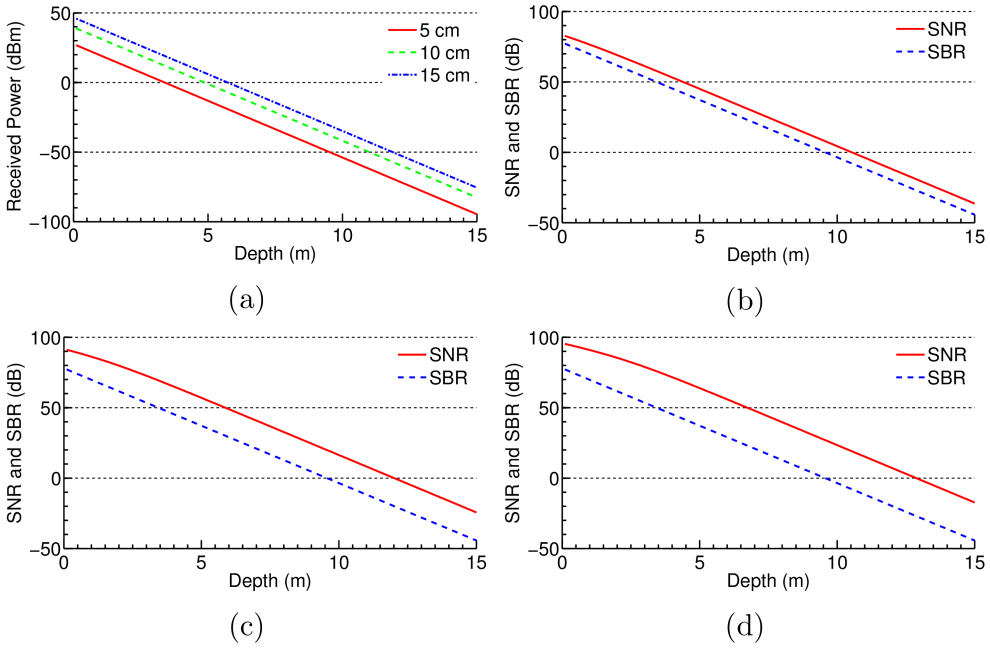

Figure 2.1: Received power (a) and SNR and SBR for a 5-, 10-, and 15-cm-diameter aperture and 5-mrad FOV (parts (b), (c), and (d), respectively). Increasing the aperture diameter provides modest improvements in SNR, although the lidar remains SBR-limited in each case.

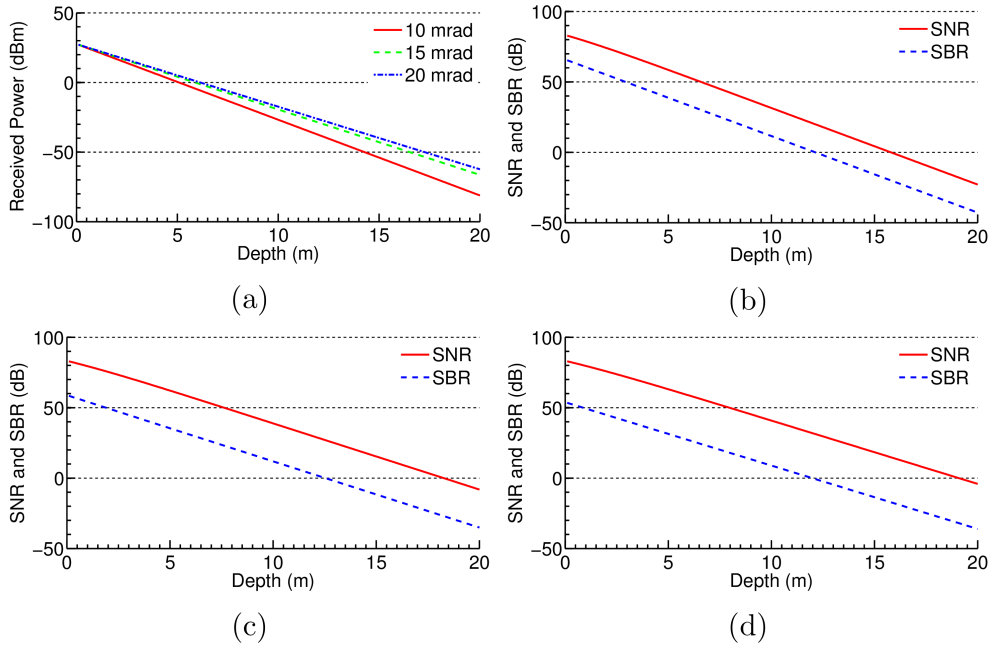

Figure 2.2: Received power (a), and SNR and SBR for a 5-cm-diameter telescope and 10-, 15-, and 20-mrad FOVs (parts (b), (c), and (d), respectively). Increasing the field of view limits the loss from multiply-scattered light.

increasing the FOV improved the performance relative to increasing the aperture diameter. Again considering only the SNR, the simulation indicated that a 5-cm-diameter aperture with a 10-mrad FOV outperformed the 15-cm-diameter aperture with a narrower 5-mrad FOV. These plots demonstrate the importance of the field of view in capturing multiply-scattered photons as was noted by Gordon [24].

Figure 2.3 shows the effects of varying the aperture diameter and field-of-view on the received power from 5, 7.5, and 10 meters in depth, again emphasizing the advantage of increasing the field-of-view versus increasing the aperture diameter.

Eye safety is an important part of field of view calculations. The single pulse exposure limit is 5 mJ/m^2 [63]. Because it is possible for a stationary observer to view two pulses as the plane passes overhead, we apply a correction factor of $N_p^{-0.25}$, where

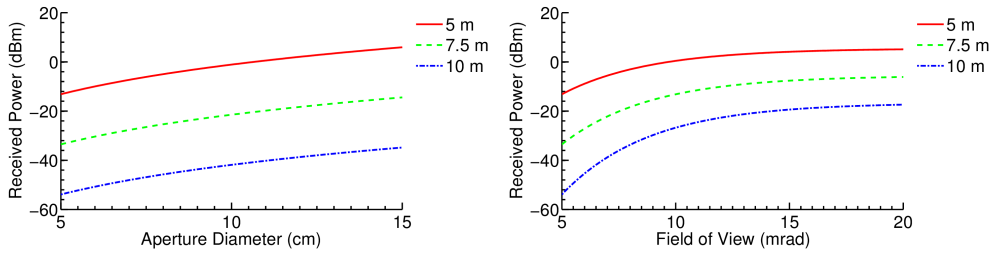

(a) (b)

Figure 2.3: Received power at 5, 7.5, and 10 meters in depth for (a) 5-15 cm aperture diameter and 5-mrad FOV and (b) 5-20 mrad FOV and 5-cm aperture diameter.

$N_p = 2$ is the number of pulses [19], yielding an eye safety limit of 4.21 mJ/m^2. For our laser the pulse energy is 26.8 mJ and our nominal flight altitude is 300 meters. Without expansion the laser beam divergence is 5 mrad, which gives a spot area of 1.75 m^2 on the water surface and a laser energy of 15 mJ/m^2, above the eye safety limit calculated above; however, expanding the beam to 15 mrad yields a laser energy of 1.7 mJ/m^2, below the calculated limit.

Our instrument operates at a 5- and 15-mrad FOV, with matched laser divergences. The narrow FOV is used to study the lidar attenuation coefficient in water as more it closely approximates the beam attenuation coefficient [24]. The wide FOV is used to study fish and plankton because of its greater depth penetration. Section 2 discusses the precautions we take in the narrow FOV configuration when the laser beam is not eye safe.

SNR and SBR for Lake Trout

We wanted to verify that the lidar would be able to detect spawning lake trout in local lakes. During the several-week spawning season in the fall, lake trout congregate in large groups at spawning sites close to the surface, at depths of just a few meters. Preferred spawning sites are rocky shoals, devoid of vegetation, and the fish will

habitually return to the same site each year [2, 64–69]. This behavior is the key that allows lidar to locate their spawning sites, and is also why knowledge of the location of their spawning sites is of such importance in controlling their population.

Churnside performed a detailed study of the lidar backscatter from sardines and developed equations to compute the cross-sectional area A_f and backscatter coefficient β_f of fish, which we used here to model the lidar signal from a lake trout [42].

For lake trout, we chose a reflectivity $\rho = 0.146$, which is a worst-case number for ocean fish, as similar data for freshwater fish are unavailable [22]. 53 cm was chosen for the length L, which is a representative number from Yellowstone Lake [8]. Using the model from Churnside, we computed a backscatter coefficient $\beta_f = 0.0016$ m^{-1}sr^{-1}. The lidar signal was again computed using Equation (2.1) with β_f substituted for $\beta(\pi, z)$ and multiplied by a correction factor of A_f/A_b where A_b is the area of the beam at the fish depth, as only part of the beam illuminates the fish.

SNR was defined as

$$\mathrm{SNR_{dB}} = 10 \cdot \log_{10}\left(\frac{P_{\mathrm{fish}}}{P_{\mathrm{shot\ noise}} + P_{\mathrm{quantization\ noise}}}\right), \tag{2.6}$$

where P_{fish} is the power reflected from the fish. SBR was defined as

$$\mathrm{SBR_{dB}} = 10 \cdot \log_{10}\left(\frac{P_{\mathrm{fish}}}{P_{\mathrm{background}} + P_{\mathrm{dark\ current}}}\right). \tag{2.7}$$

Other parameters were the same as in Table 2.1. The results for a single lake trout and a 5-cm-diameter telescope and 5- and 15-mrad FOVs are displayed in Figure 2.4. Figure 2.5 displays the same plots for 20 lake trout. Because the beam is a significantly larger than a fish, increasing the beam FOV is not without cost. For a single lake trout the 15-mrad wide FOV configuration is background limited at all depths, and for 20 trout it is background limited at approximately 6 meters. However, narrowing

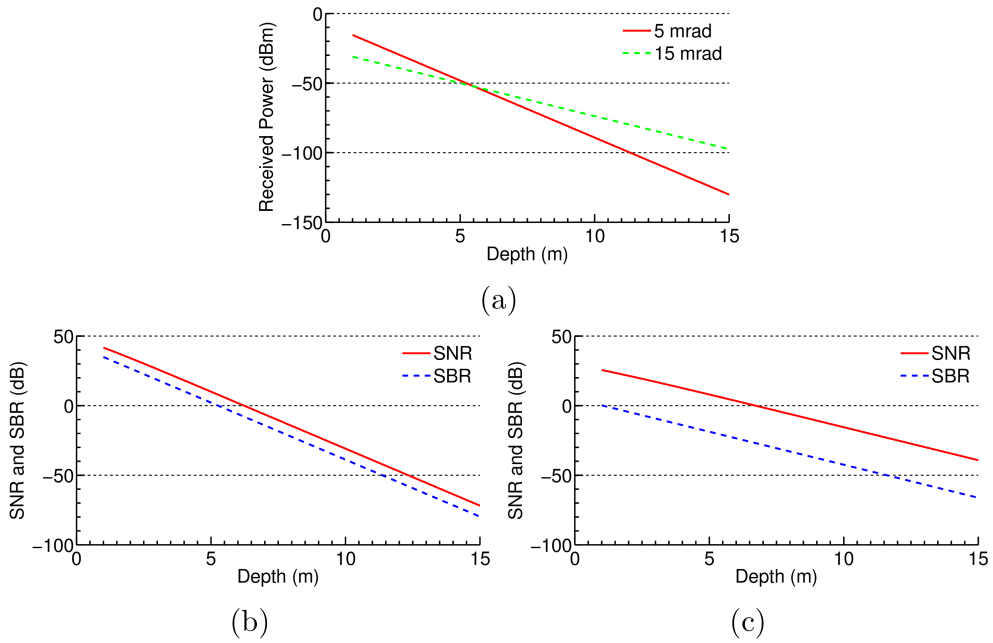

Figure 2.4: Received power (a) and SNR and SBR plots for a single lake trout, 5-cm-diameter telescope and 5- and 15-mrad FOVs (parts (b) and (c), respectively).

the beam decreases the amount of water surveyed, and the wide FOV configuration covers nearly 8 times more area than the narrow FOV. Thus, the wide FOV is still used for fisheries surveys. Figure 2.6 shows the signal power received from a single lake trout at various depths while varying the FOV. The figure follows the same pattern as Figure 2.3.

Coaxial Receivers

Many dual-polarization lidars use a single optical assembly with some method of separating polarizations, typically a polarizing beamsplitter cube, liquid crystal variable retarder [70], or other method of discriminating co- and cross-polarization.

We chose to use two separate co- and cross-polarization receivers mounted side by side. Optically, this makes the receivers simpler but increases the difficulty of

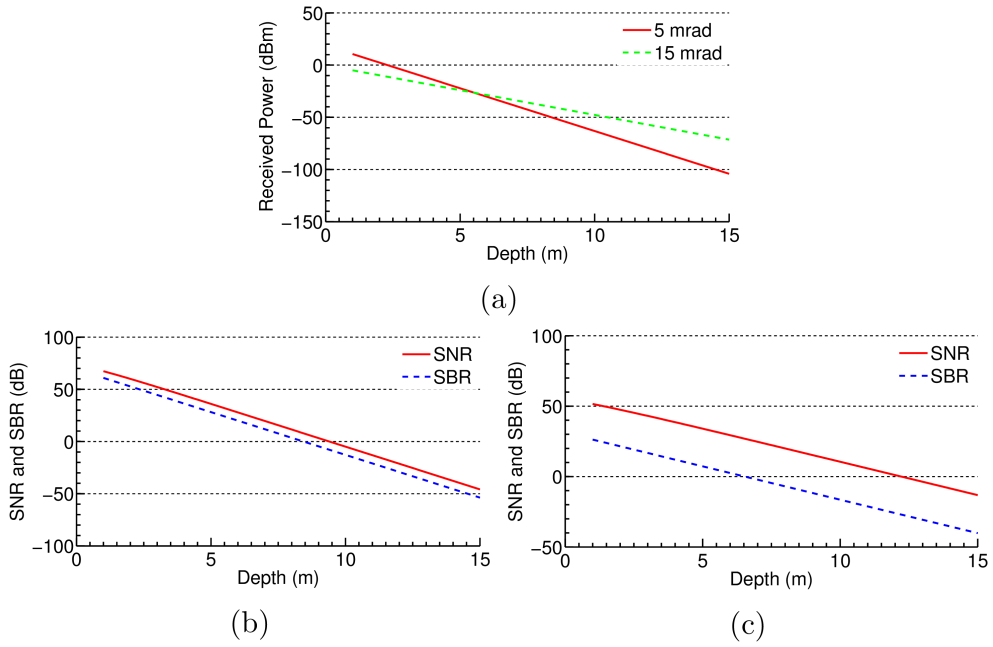

Figure 2.5: Received power (a) and SNR and SBR plots for 20 lake trout, 5-cm-diameter telescope and 5- and 15-mrad FOVs (parts (b) and (c), respectively).

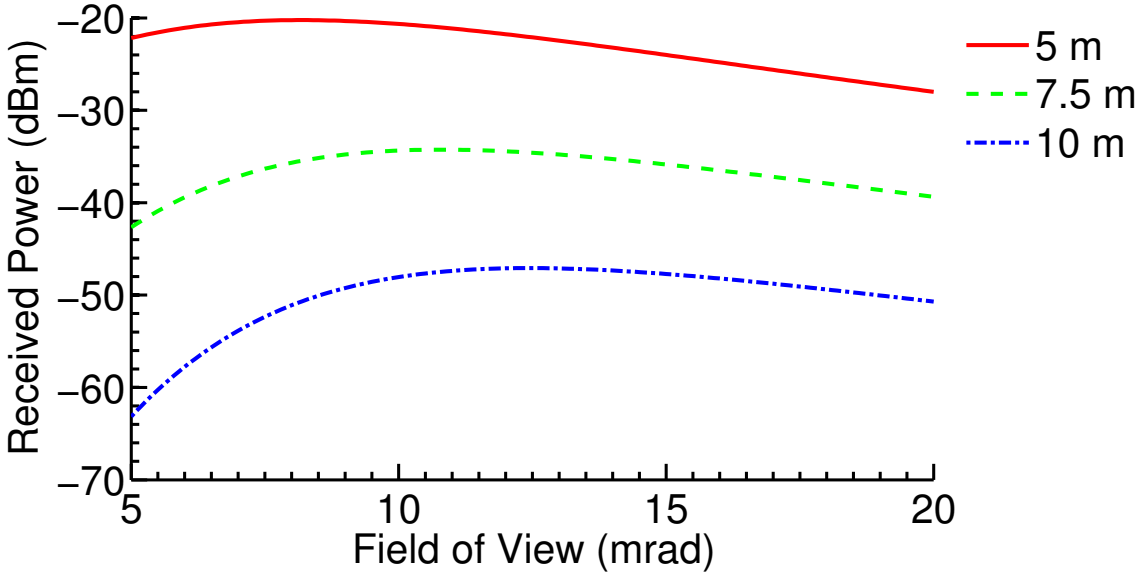

Figure 2.6: Received power from 20 lake trout at 5, 7.5, and 10 meters in depth for a 5-cm aperture diameter and a 5-20 mrad FOV. The results are similar to those computed for water (Figure 2.3 on page 17); however, the maximum power at deeper depths is obtained at a FOV of approximately 12.5 mrad.

aligning and calibrating the lidar. Because of this, alignment is performed on the ground at a test range, and calibration is performed in a lab. Alignment while in the air is not feasible due to variations in the signal from the water surface and because the small size of the plane makes it difficult to adjust the lidar while in flight. This raises the concern of the lidar losing alignment during flight and being unable to correct it; however, this has yet to happen.

Each receiver was radiometrically-calibrated separately using an integrating sphere. The purpose of this calibration was to determine the PMT output voltage for a given radiance at the receiver aperture and a given PMT gain value. This was necessary to determine in order to make comparisons of the data between the receivers because the co- and cross-polarized receivers had different aperture diameters, and also because the two PMTs would be expected to have slightly differing responses.

The complete receiver with the polarizer attached was placed directly in front of the integrating sphere aperture in a darkened lab. The light output of the sphere is randomly-polarized, and it was cycled through a series of radiance values, and at each value the PMT output was recorded as the PMT gain voltage was varied. Each receiver configuration was tested. We then calculated a fit to a 4x1 calibration polynomial, which was chosen as it most closely represented the data, given below.

$$L_e = p_{00} + p_{10}g + p_{01}y + p_{20}g^2 + p_{11}gy + p_{30}g^3 + p_{21}g^2y + p_{40}g^4 + p_{31}g^3y, \qquad (2.8)$$

where L_e is radiance measured in $\mathrm{Wcm^{-2}sr^{-1}nm^{-1}}$, g is PMT gain in volts, y is the PMT output in volts, and p_{xx} are the calibration gains. This model fit the wide FOV receiver responses better, with $R^2 > 0.9$ for each channel. The fit to the narrow FOV receivers was not as good, with $R^2 > 0.7$. This appeared to stem from the light output from the integrating sphere being too weak at lower PMT gain values.

Tilt Angle

Marine lidars are typically operated at a small angle from nadir to reduce the unwanted specular reflection from the water surface, which is often very large and can saturate the co-polarized receiver. To determine the optimum tilt angle, we performed a simple simulation where we considered the laser as a single ray pointed at the surface (without divergence). Using the calibration discussed in the previous section, we computed the amount of light at each receiver necessary to saturate the digitizer. We then calculated ϕ_{sat}, how far in radians outside the field of view ϕ_{FOV} the laser beam could fall while saturating the receivers.

To model the distribution of wave slope angles, we used the Gram Charlier distribution from Cox and Munk [71]. Shaw and Churnside showed that the Cox and Munk distribution is valid for near-neutral conditions (i.e., equal air and water

temperatures), but that it underestimates surface roughness with negative stability (water warmer than air) [72]. We assumed the worst-case scenario where the receiver tilt is aligned with the wind direction. σ_u^2 was calculated using the "clean surface" equations, as are the skewness and peakedness coefficients. We then computed the probability that a wave slope falls within the saturation angle

$$\theta_{\text{sat}} = \theta_{\text{lidar tilt}} \pm (\phi_{\text{FOV}} + \phi_{\text{sat}}) , \tag{2.9}$$

where $\theta_{\text{lidar tilt}}$ was the lidar head tilt angle. This probability is then used in a binomial experiment to determine the probability of saturation in a given time period, assuming the lidar is run at 50 shots per second (the typical repetition-rate in practice). Results are shown in Figure 2.7 for wind speeds from 1-20 m/s and lidar tilt angles from 5-30°.

From the simulation we chose 15° as our lidar tilt angle, but the system was designed so that this angle is adjustable. Increasing the angle beyond 15° would lessen the probability of saturation, but could possibly eliminate the surface return altogether, in which case our surface detection algorithm would fail. At a 5 m/s wind speed and 4V gain voltage the probability of the co-polarized receiver not saturating in five minutes is 0.94 (min/max radiance is 0.02 and 710 $\text{Wcm}^{-2}\text{sr}^{-1}\text{nm}^{-1}$, respectively) and the probability of the cross-polarized receiver at a 3.5V gain voltage not saturating is 0.91 (min/max radiance is 0.02 and 465 $\text{Wcm}^{-2}\text{sr}^{-1}\text{nm}^{-1}$, respectively), which was acceptable for our purposes. We have not experienced significant problems with saturation at 15° in practice. Due to safety concerns, we do not fly if surface wind speeds exceed 7 m/s.

Final Optical Design

Figure 2.8 shows the cross-polarized receiver layout in ZEMAX. Figure 2.9 shows a picture of the receiver side of the lidar head, and Figure 2.10 shows the laser which

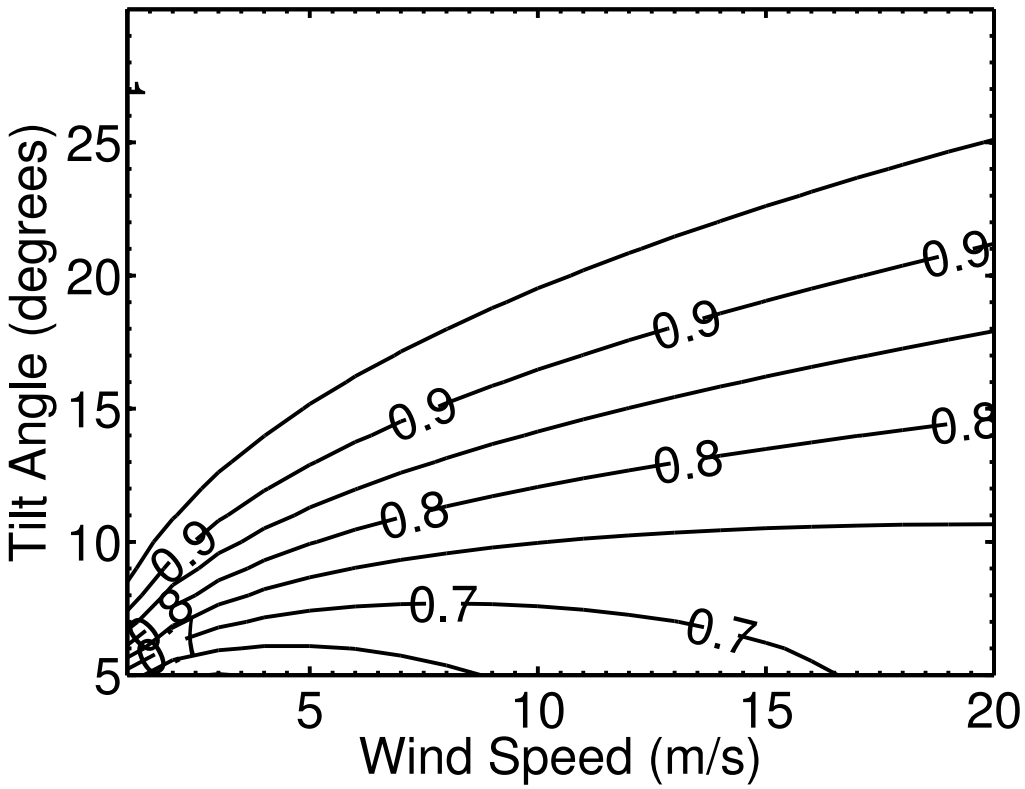

Figure 2.7: The probability of the co-polarized receiver at 4 V gain voltage not saturating in five minutes at wind speeds from 1-20 m/s and tilt angles from 5 to 30 degrees. In the final design we chose 15° as our tilt angle.

is mounted on the opposite side of the receivers. Each receiver is mounted to an aluminum rail, which can be adjust to align the lidar by loosening the two mounting screws. These screws are undersized for the breadboard mounting holes to allow for a small amount of adjustment for coarse alignment. Fine alignment is accomplished by adjusting the position of the receiver aperture in x and y. For the wide FOV configuration, the co-polarized front lens is a LA1417-A from Thorlabs with a 150 mm focal length and the cross-polarized lens is a LA1353-A from Thorlabs with a 200 mm focal length. The rear lens in both configurations is a KPX085 from Newport with a 62.9 mm focal length. Full details of both the wide and narrow FOV designs are available in their respective ZEMAX files.

To change FOVs the front lens is changed by removing the front lens barrel from each receiver and installing the new FOV lens barrel. This allows the FOV to be changed quickly in the field. Witness marks are used to ensure that the polarizers are installed at the same rotation.

Initially the lidar was designed with a 5-cm-diameter co-polarized aperture and 5-mrad "narrow" FOV (e.g. undiverged laser beam). The crosspol aperture diameter was increased to 7.5 cm to better capture the typically weaker cross-polarized signal. After simulation and field studies proved the narrow FOV was inadequate the capability to operate at a "wide" 15-mrad FOV was added. This was achieved by placing a negative diverging lens in front of the laser and changing out the receiver telescopes. The optical system was designed so that this can be accomplished without adjusting the alignment, and calibrations are performed for both FOVs. A FOV "swap" can be performed on the ground in approximately 30 minutes.

Because the narrow-FOV configuration is not eye safe it is not operated near people or animals. During most flights this does not present a significant impediment, as the lakes we study are remote and typically have little to no human activity.

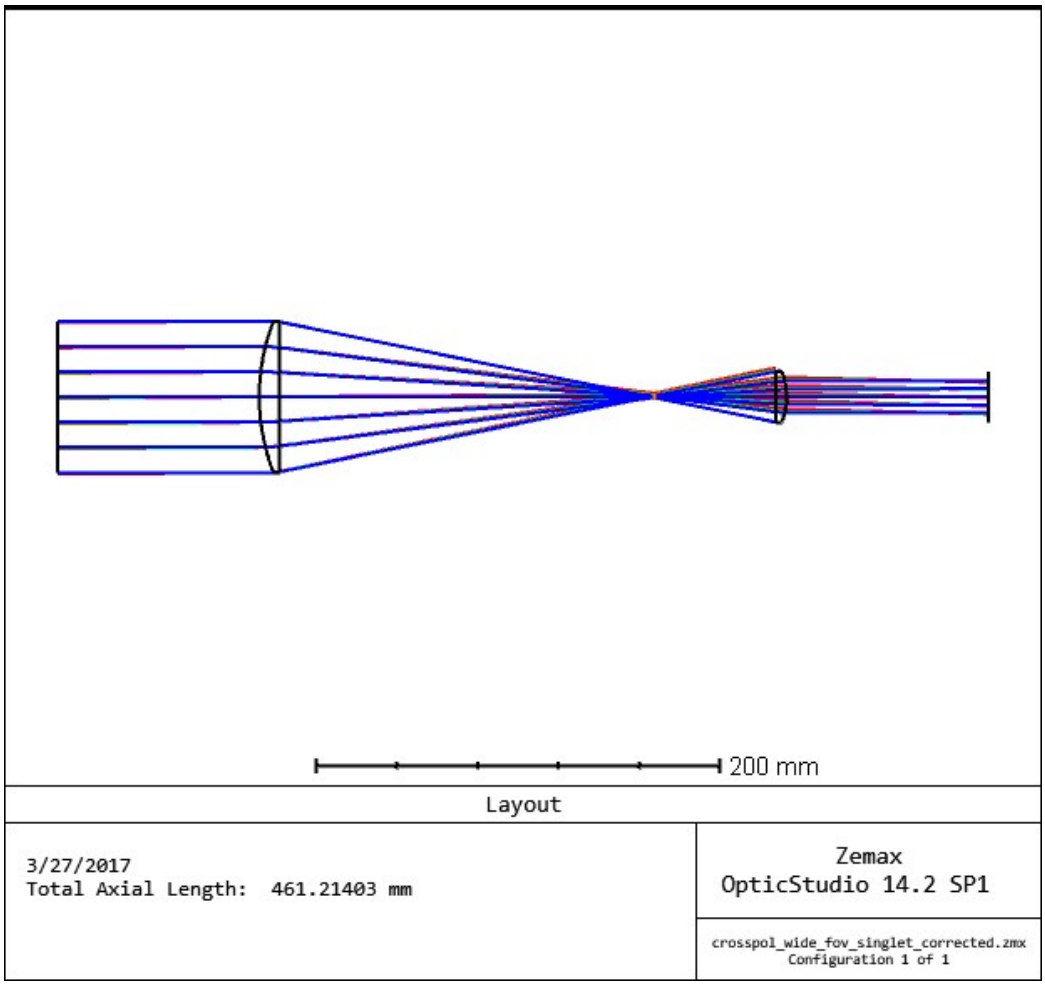

Figure 2.8: The layout of the cross-polarized receiver in ZEMAX. The co-polarized receiver is of the same basic design.

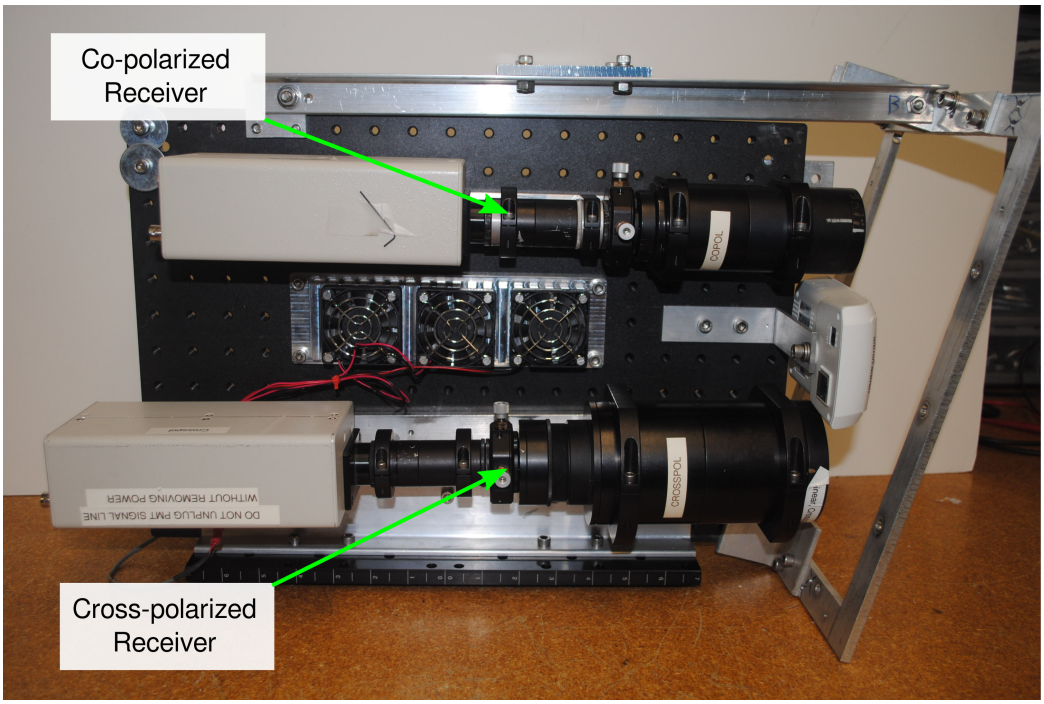

Figure 2.9: A picture of the lidar head, showing the co- and cross-polarized receivers.

During flight the pilot constantly monitors for people/animals and other hazards on the surface, which are easily identified and avoided because of the low flight altitude. These precautions are not necessary for the wide-FOV configuration.

The current system is not scanned, and the receivers and laser are held in a fixed orientation to the plane. This first system was intended as a proof-of-concept to investigate the possibility of studying freshwater ecosystems with lidar. A scanner system would increase the complexity, cost, and size of the system, but could be added in the future.

With knowledge of the phase function of the scatterer and the laser output energy the volume scattering function β could be computed from the received lidar signal. A correction factor would have to be determined as the calibration source is Lambertian. This calculation would be the scattering phase function of interest divided by the Lambertian phase function of $\tilde{\beta}_L(\phi) = cos(\pi - \phi)$ in the backscatter

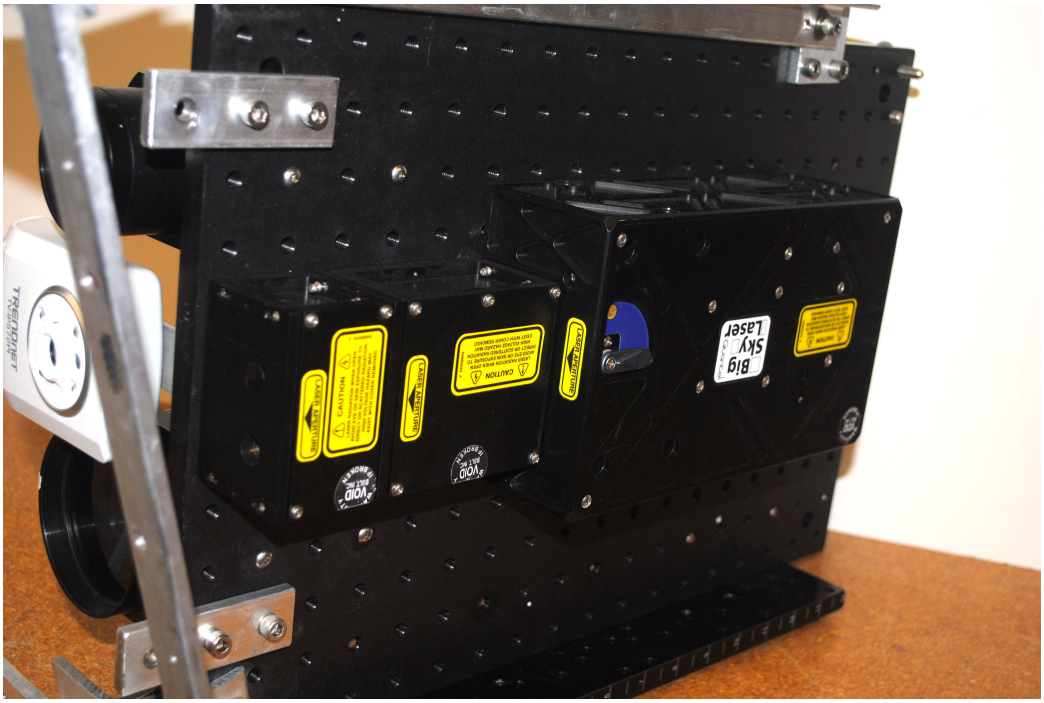

Figure 2.10: A picture of the lidar head, showing the laser mounted opposite the receivers.

direction. Note the factor of π is present because the phase function is corrected to be in the backscatter direction and this function only exists between $\pi/2 < \phi \leq \pi$ and is 0 otherwise.

Currently, we are limited by the background light. To reduce the background light, the current laser line filter (with a 1.5 nm bandwidth, the limit of what is readily-available commercially) could be replaced with a narrower-bandwidth filter. However, care would have to be taken because of the filter's angle dependence (referred to as "angle tuning"). As the angle of incidence increases from normal on a dielectric filter, the filter's response shifts to shorter wavelengths. This effect is described by the following equation,

$$\lambda(\theta) = \lambda(0)\sqrt{1 - \frac{\sin^2(\theta)}{n_{\text{eff}}^2}}, \tag{2.10}$$

where $\lambda(\theta)$ is the wavelength at the angle of incidence, θ, $\lambda(0)$ is the wavelength at normal incidence, and n_{eff} is the effective attenuation coefficient, which is different for each filter and polarization state. Here we assume $n_{\text{eff}} = 1.5$ and an angle of incidence of $\theta = 22.5$ mrad, which was determined by multiplying the receiver FOV half-angle (7.5 mrad) by the telescope beam expander ratio of 3. This results in a wavelength shift of 0.06 nm, which is negligible at this FOV.

Dynamic Range and Digitizer Considerations

Dynamic range is an important consideration in lidar design. Older designs typically used either a logarithmic amplifier or two separate digitizers to achieve an acceptable dynamic range, as high-speed digitizers were limited to eight bits. Designs using logarithmic amplifiers suffer from the challenge of calibrating the amplifiers and large quantization noise for larger signals. Using multiple digitizers also requires careful calibration and attention to matching the phase, frequency, and amplitude responses of each digitizer.

Modern digitizers are just becoming available with high sample rates and larger bit depths. For our project we chose to use a GaGe CS148001U 14-bit, 800 MSPS USB digitizer from GaGe Applied (Lachine, QC, Canada). This digitizer has an ideal dynamic range of 86 dB, but when the effective number of bits (ENOB) is considered the actual dynamic range is only 69 dB, corresponding to an ENOB of 11.2, which provides penetration depth to close to the SNR-limit of the 5-cm-diameter aperture, 15-mrad FOV optical design.

Trigger Generation, Computer Interface, and Power Supply

A custom-built trigger generator using a Xilinx Spartan-6 FPGA (San Jose, CA) allowed a USB-programmable variable delay to gate the PMTs and trigger the digitizers. Careful attention was paid during FPGA design to ensure a worst-case timing skew between trigger outputs of 171 ps (as reported by the FPGA synthesis software), which would equate to a worst-case offset of 2 cm between channels. A 64 MHz clock frequency provides a delay resolution (in air) of 4.7 meters, with a minimum delay of 65 meters. Because the trigger delay is programmable, we minimize extraneous data captured by the lidar and enable it to be easily adjusted for different flight altitudes.

All the hardware was designed to interface with the computer via USB and the entire lidar was controlled from a laptop with one USB cable. This minimizes the amount of cabling in the aircraft cabin and simplified installation. We have, however, experienced some difficulties with the limited data bandwidth of USB 2.0. If the laser was operated at the full 100 Hz pulse repetition frequency (PRF) we missed lidar shots because the samples could not be transferred quickly enough to the computer. To avoid this, the laser was operated at a reduced 50 Hz PRF, which still provided sufficient shot overlap at a 44 m/s flight speed. Upgrading to USB

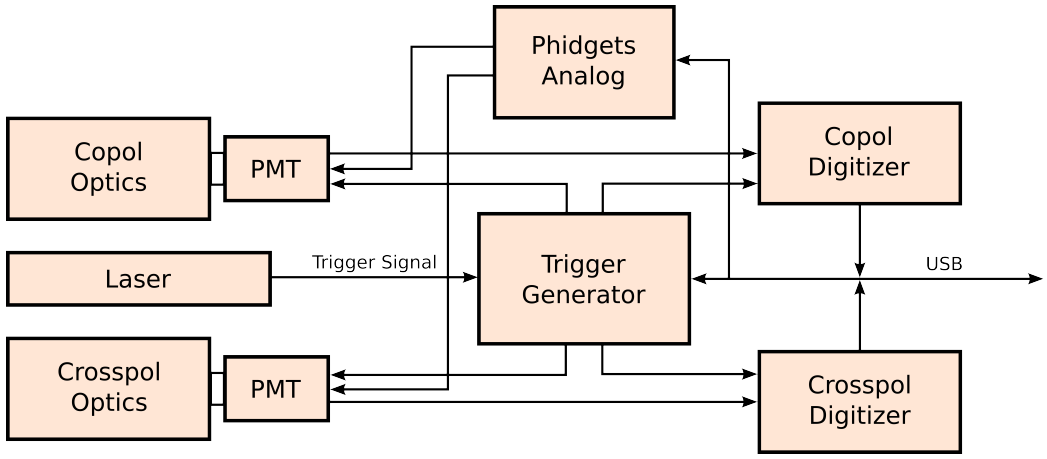

Figure 2.11: Block diagram of the major electronic components of the lidar system.

3.0 would solve this problem and allow us to fly at a greater speed, but USB 3.0 digitizers were not available when the system was designed. Figure 2.11 is a block diagram which illustrates the major electronic components of the lidar system.

Despite the higher electrical efficiency of the diode-pumped laser the power requirements for our lidar still exceeded what has been available from single-engine aircraft that were not able to provide high electrical output. To power the lidar we used a 12 V, 92 AH deep-cycle battery and a 600 W, pure sine-wave, regulated AC inverter. This configuration was able to power the lidar while collecting data for approximately two hours.

Synchronization

A major task was synchronizing each piece of hardware and the software because each component was designed to operate asynchronously. The digitizers were synchronized to each other using an Abracon SYNC-10 portable 10 MHz frequency reference (Irvine, CA) and a -3 dB splitter, with matched cables feeding each digitizer.

The computer was synchronized to GPS time using a Time Machines TM1000A GPS Time Server (Lincoln, NE). Each incoming piece of data was then timestamped

by the computer as it arrives so that it can later be matched with the corresponding GPS location.

To synchronize the digitizers to the computer time a feature of the GaGe digitizers was enabled that timestamped each shot from a given "epoch", which is set by the computer. Each shot can then be associated with a matching shot from the other digitizer, and timestamped by the computer.

Operating Software Design

The software is divided into two major pieces, the application software which runs the lidar in the air, and the post-processing software which generates the images for analysis after a flight.

The application software allows the operator to troubleshoot errors and monitor the operation of the lidar during flight, but does not perform any analysis of the data. During the hardware selection we took note of the programming libraries available for each component, and selected C# .NET as the development language for this software program as all the hardware had libraries in this language.

The software allows the operator to monitor the operation of the lidar and adjust the laser PRF, PMT gains, and trigger altitude. Both single shots and an "echosound" plot are displayed, as well as the laser status, temperature, and the GPS location.

Data were stored on the fly in a SQLite database. SQLite was chosen over a "flat-file" storage scheme due to the ease of programmatic access and implementation, with minimal overhead. The application stores the raw data, PMT gains, trigger altitude, and the time for each shot. Laser PRF, sample rate, and laser head tilt angle along with remarks for each run are stored in a separate configuration table. A third table stores the calibration parameters; however, data are not stored calibrated to prevent a mistake in the calibration parameters from ruining data from a run. Each shot has

a cross-reference to the related entry in the configuration and calibration table. GPS data were stored in a separate table with both a computer and GPS timestamp, to guard against errors in either corrupting a data run and for comparison.

Post-Processing Software Design

After completing a lidar run the data stored in the database were processed using a Python application which converted the digital number to radiance, calculated the exact location and altitude of each shot, and also computed the location of the water surface and the depth increment for each sample.

The water surface was identified using a basic algorithm which locates the maximum signal peak in the co-polarized channel and then walked "backward" in the direction of the lidar to 1% of this maximum value. This algorithm is intended to locate the leading edge of the surface return pulse, which is used as the reference point for the surface. The leading edges of pulses from other targets (fish, the bottom) are then located relative to this point. While this algorithm may fail when the surface return is weaker than the volumetric scattering from the water immediately below the surface [40], our lidar is not intended to perform high-accuracy bathymetry, and a low-cost solution was preferable to other proposed solutions to this problem such as a separate infrared or Raman channel requiring an extra receiver and associated hardware [41]. This is a capability that could be added in the future by unblocking the 1064 nm output of the laser.

Each shot location was calculated using coordinates from a commercial GPS receiver with Wide Area Augmentation System (WAAS) capability. The location of shots taken between position fixes was interpolated.

Shots were assembled into false-color images, an example of which is shown in Figure 2.15 in Section 2. These images were examined qualitatively for the presence

of fish or plankton; no automated algorithms to detect these organisms in freshwater are known by us to currently exist [47].

Comparison to the NOAA Fish Lidar

Churnside has developed an airborne lidar for oceanic ecosystem studies, the "NOAA Fish Lidar" [18, 43, 45, 46]. This lidar shares many similarities with the lidar that we described here, and was the basis for our design. A 532 nm flash-pumped Nd:YAG laser is used, which produces 12 ns, 100 mJ pulses at a pulse repetition frequency of 30 Hz. The co-polarized receiver aperture diameter is 6 cm, and the cross-polarized receiver aperture diameter is 15 cm. Field of view is 16 mrad, slightly larger than the 15 mrad wide field of view of our lidar. Over the years the NOAA lidar has evolved to incorporate two receivers to measure both co- and cross-polarized radiation and has been reduced in size to where it can be flown in a four-seat Cessna 177, very similar to the Cessna 185 in which our lidar operates [45].

There are some differences between the two. Our lidar uses a diode-pumped laser for its higher electrical efficiency and shorter pulse width. This laser has a lower pulse energy, but is able to operate at a higher PRF (up to 100 Hz). The NOAA lidar uses a logarithmic amplifier paired with a 1 GSPS, 8-bit digitizer to achieve a dynamic range of approximately 40 dB. Because of the larger bit depth of our digitizers we are able to directly sample the lidar signal without the need for an intermediate logarithmic amplifier, and achieve a larger 69 dB dynamic range. This simplifies the overall system.

The NOAA system uses an embedded high-speed computer to digitize and process the data, which allows the use of PCI-Express (PCIe) digitizers. This avoids the problems we have encountered with USB digitizers, which we are limited to because we designed our entire lidar system to be run off a single laptop. PCIe

digitizers are numerous, while high-speed USB digitizers are still fairly rare. We may move to PCIe digitizers in the future to get around the USB bandwidth bottleneck.

Experimental Results

The lidar we have described has been successfully flown over Flathead Lake in Montana and Yellowstone Lake in Yellowstone National Park, and several other local lakes in Montana. Figure 2.12 shows the lidar mounted in the rear of a Cessna 185. Potential lake trout spawning sites are qualitatively identified by the authors through examination of the data. Prior work where lidar data were compared with echosounder data has shown that fish typically appear as long spikes because of the long laser pulse [18, 20, 23, 42]. Potential spawning sites are identified by considering the location and depth of the fish. No automated algorithms for freshwater fish identification currently exist, and this is an area for future research.

Figure 2.13 shows an example lidar shot from Yellowstone Lake in clear water. The return from the water usually falls below the receiver noise at about 10 meters in the cross-polarized trace, which is fairly close to the 12 meters predicted in simulation. The optical properties used to develop the SNR and SBR simulations had to be estimated or were measurements taken from similar bodies of water. Often, the only optical properties available for a given lake are Secchi disk depths[1]. Secchi disk depths are rough estimates of the water optical properties because of the qualitative effect of needing a human observer, and they are also dependent on lighting conditions and the meticulousness of the observer [73, 74]. Measurement of local freshwater lake trophic and optical properties may reduce this discrepancy as assuming parameters from

[1] A "Secchi disk" is a circular disk with an alternating black and white pattern which is lowered into the water until it disappears. The depth at which it disappears is the "Secchi depth".

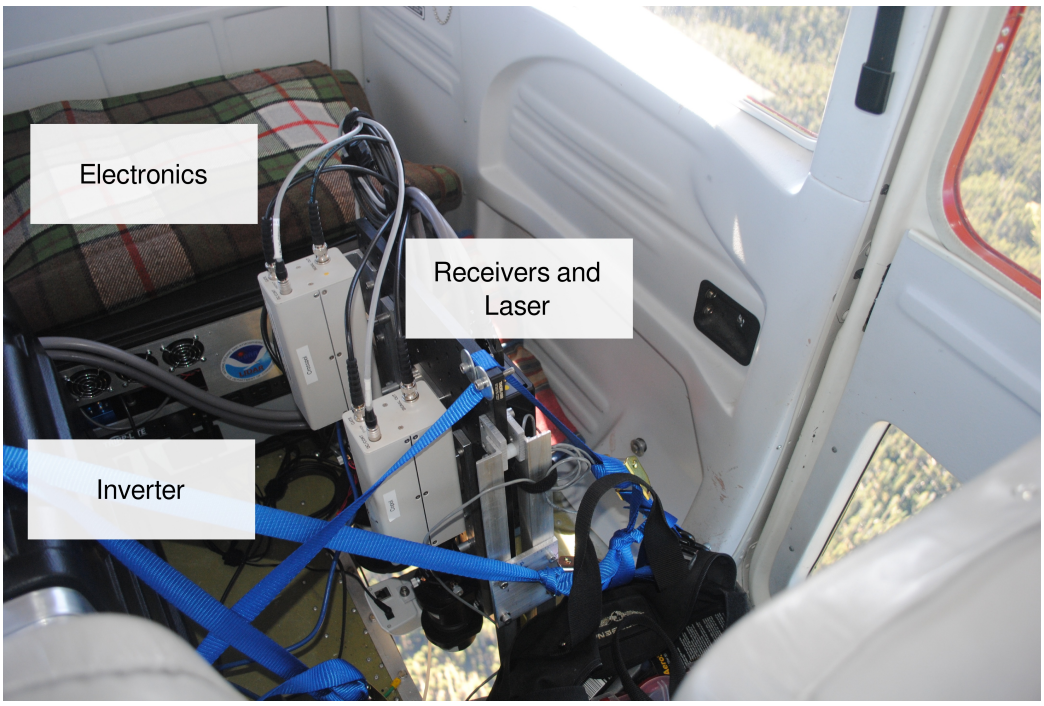

Figure 2.12: The lidar mounted in the plane. The lidar optics are mounted over a hole in the floor of the plane and tilted forward at an angle of 15 degrees to reduce the surface reflection. Behind the lidar head is the electronics case and to the left in the photo is the inverter case.

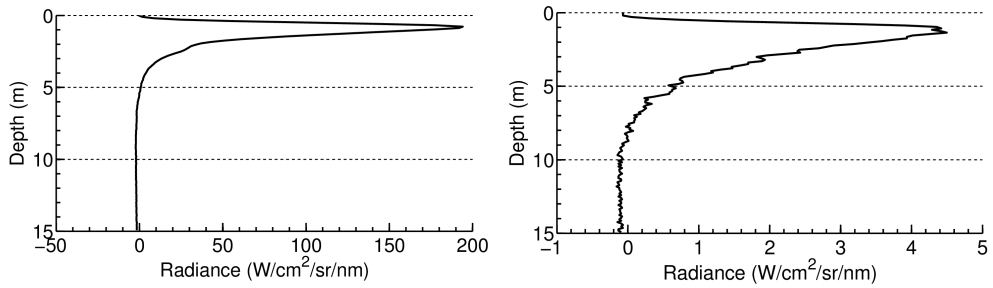

(a) (b)

Figure 2.13: A representative single lidar shot from Yellowstone Lake in clear water without the presence of fish or a shallow lake bottom. The co-polarized trace is plotted in (a) and the cross-polarized trace in (b). The maximum of the surface pulse appears at approximately 1 meter depth because the surface detection algorithm locates this maximum and then finds the point on the pulse towards the surface where the power is 1% of this maximum, which is the first part of the laser pulse reflected from the surface.

other lakes is problematic; Kirk notes that estimates for the absorption coefficient of CDOM vary widely, even for lakes in the same general area [28].

Figure 2.14 shows an example single lidar shot with the presence of fish from Yellowstone Lake, and Figure 2.15 shows an image from the cross-polarized channel of the same fish hit.

Conclusion

In this chapter we discussed the design and implementation of an airborne lidar for freshwater ecosystem studies, including the rationale behind the some of the choices we made in the optical, electronic, and software designs. SNR and SBR plots for various aperture and FOV sizes were presented. Dynamic range is often a limiting factor in lidar designs, and it is important to consider the real-world dynamic range of a given digitizer (using the ENOB) and not the theoretical dynamic range.

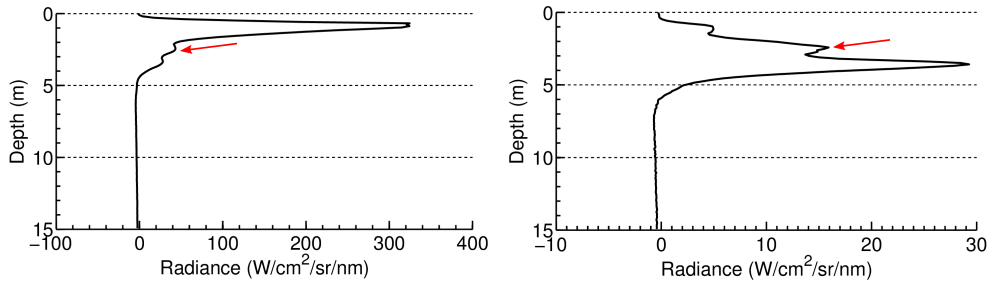

(a) (b)

Figure 2.14: An example single lidar shot from Yellowstone Lake in showing a return typical of fish and a shallow lake bottom. The co-polarized trace is plotted in (a) and the cross-polarized trace in (b). The fish appear as the bump at approximately 2.5 meters highlighted by the red arrow; the lake bottom is just below at approximately 4 meters and appears strongest in the cross-polarized channel.

With the advent of digitizers with high bit-rate and bit-depth, older approaches to increasing limited digitizer dynamic range may no longer be necessary.

Our lidar system uses two receivers, which necessitated a more complicated calibration but was a simpler and less expensive approach. Alignment is more difficult, but we have not yet encountered any major difficulties.

The biggest limitation of our instrument during these initial experiments was the limited data bandwidth of USB 2.0. Moving to USB 3.0 digitizers would allow us to run at a higher PRF, as currently we have to limit the PRF to avoid missing shots. We are also considering moving the processing and digitizers to an embedded computer system, which would allow us to use PCIe digitizers.

Since finishing construction we have completed successful flights of Yellowstone Lake, Flathead Lake, and other lakes throughout Montana.

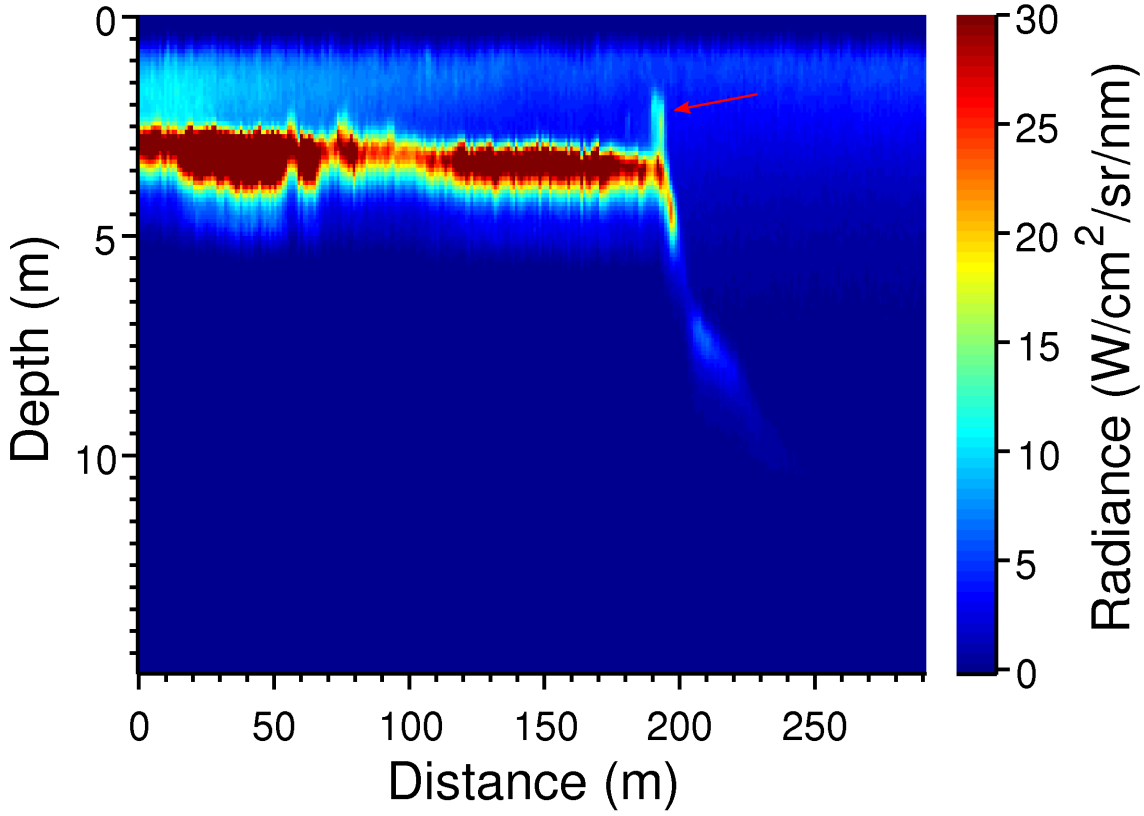

Figure 2.15: An image from the cross-polarized channel of the fish return depicted in Figure 2.14 in Yellowstone Lake. The fish are indicated by the red arrow.

DETECTION AND MAPPING OF INVASIVE LAKE TROUT

This chapter draws largely from [75].

Introduction

In this chapter we present the use of an airborne lidar for identifying potential lake trout spawning sites. Airborne lidar can be used to locate groups of fish, and thus can be used to identify possible spawning sites in a manner similar to that done with acoustic tracking [10, 13]. Airborne lidar has been demonstrated for detecting and profiling fish in the open ocean [14–19]. The data produced are similar to what would be obtained from a traditional acoustic echosounder [20, 21]. With calibrated laboratory measurements of the reflectivity of fish species of interest, accurate estimates of biomass can be made from lidar data [20,22,23]. Using airborne lidar for fisheries surveys allows larger areas to be rapidly mapped and at vastly lower cost than with a surface vessel [18]. A typical flight can map 80 km of water per hour with a 5 meter swath, and costs only $500 per hour. Data are often available within 24 hours of the flight. While airborne lidar has been used in the ocean for fisheries surveys, the technique has not been well studied in lakes.

Experiments

2004 Flight

An initial experiment was conducted in 2004 to explore the feasibility of using lidar to locate lake trout spawning sites in Yellowstone Lake [47]. The experiment took place from September 18-24 at the peak of the lake trout spawning season using the National Oceanic and Atmospheric Administration (NOAA) marine lidar [18]. This lidar operated at 532 nm with a 100 mJ pulse energy and pulse repetition frequency

(PRF) of 30 Hz. At the time this instrument only measured co- or cross-polarized energy. We selected cross-polarization owing to the greater contrast it offers between fish and scattering material in the water. The beam spot diameter on the water was five meters and the lidar was mounted to point 15° off nadir to reduce unwanted reflection from the surface. The typical flight altitude was 300 meters but portions of the flight were run at 150 meters.

Due to inclement weather we were only able to fly on September 21. Much of the flight concentrated on the West Thumb area but several loops were made around the periphery of the lake, focusing on shallow areas, to identify as of yet unknown lake trout spawning locations.

We selected grayscale time-depth images to display the data (Figure 3.1) to better identify fish. In Figure 3.1, fish hits at the edges of an underwater cliff are indicated by the red arrows. The clusters of fish appear as vertical lines, caused by the temporal spread of the laser pulse, floating above the bottom.

Each image was examined for the presence of fish. Fish were identified based on prior work showing the expected lidar return from fish schools [23]. Lidar shot numbers were recorded, matched to GPS coordinates and mapped (Figure 3.2). Several of the hits found in 2004 were later corroborated by Park Service officials to be lake trout spawning sites. The hits in the northeastern part of the lake were in an area where lake trout are not known to exist and have been postulated to be from underwater thermal vents. Using data from the 2004 lidar flight, lake trout were caught in 2007, one of which is shown here (Figure 3.3) at approximately 62 cm in length with at least eight juvenile cutthroat trout in its stomach.

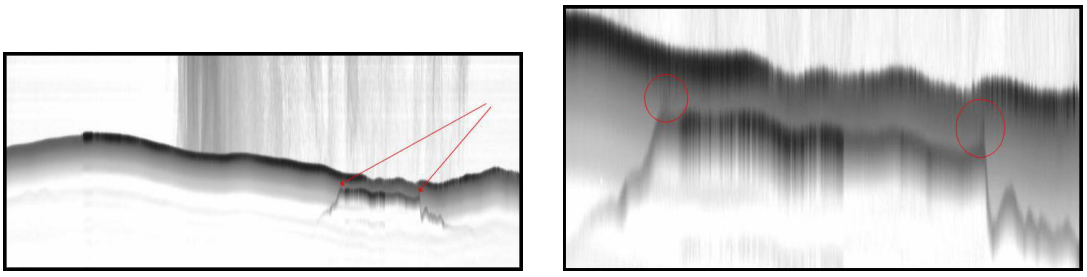

(a) (b)

Figure 3.1: On the left is a time-depth profile of airborne lidar from the Southeast Arm of Yellowstone Lake. Depth is shown on the vertical axis, increasing from top to bottom, and time is shown on the horizontal axis, increasing left to right. Strong signals are shown in black, whereas weak or absent signals appear as white. The arrows point to fish hits. The surface of the water appears wavy because it has not been corrected for the motion of the plane. Above the bright surface return is air, which exhibits scattering from snow that was present during the flight. The image is a composite of 500 lidar shots, covering 16.7 seconds or roughly one kilometer of flight. To the right is a close-up image of the fish hits shown to the left.

2015-2016 Experiments

During 2014 and the spring of 2015 we developed a new lidar at MSU for use in airborne studies of marine ecosystems. This lidar is very similar to the NOAA lidar used in 2004 with a 532 nm wavelength, variable 1.5-5 meter diameter spot size, higher 100 Hz PRF, but smaller 26.8 mJ pulse energy. Modeling indicates that it should be able to detect lake trout up to 10 meters in depth. The new lidar is capable of making simultaneous measurements of both co- and cross-polarized energy and was designed to fit in a smaller Cessna 185 'Skywagon' aircraft [26].

On September 23, 2015, during the peak of the lake trout spawning season, we undertook a flight of Yellowstone Lake to identify possible lake trout spawning locations with the MSU lidar. The flight altitude was 300 meters, and the spot size on the water was 1.5 meters in diameter.

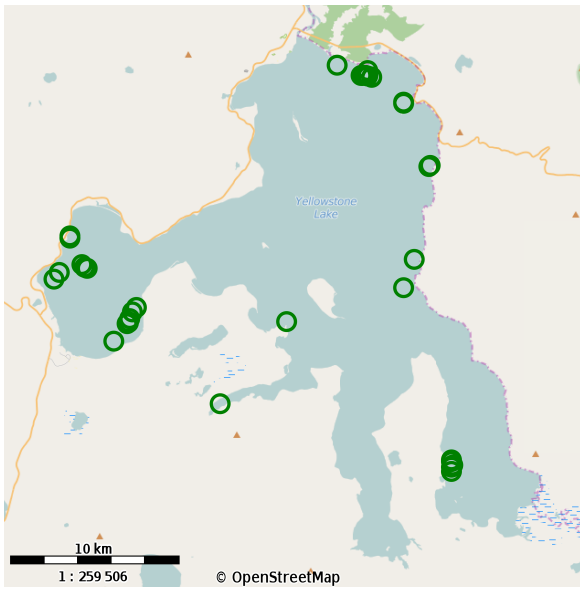

Figure 3.2: Map of fish hits from the 2004 flight. Each hit is shown as a green circle. The fish hits in the West Thumb area of the lake were not surprising; however, the hits in the Southeast Arm were at that time previously unknown populations of lake trout but in an area where Park Service models had predicted lake trout would be. In 2007 a National Park Service fisheries boat with gillnets traveled to the location discovered by the lidar and caught many lake trout, a valuable validation of the lidar-generated map. Top of the map points north. Map data © OpenStreetMap contributors.



Figure 3.3: One of many lake trout caught in 2007 in the Southeast Arm at a site with a large group of fish identified by lidar. Its stomach contains juvenile cutthroat trout. Photograph courtesy Stacey Stigler, National Park Service.

Table 3.1: Fish Hits – 2015

Latitude (°)	Longitude (°)	Fish Depth (m)	Bottom Depth (m)
44.463335	-110.553848	1.50	2.50
44.464609	-110.553092	1.50	3.00
44.466968	-110.548557	1.50	3.00
44.443815	-110.461653	2.00	4.00
44.296847	-110.335097	2.00	2.50
44.284366	-110.321137	1.00	2.00
44.313308	-110.268721	1.00	2.00
44.309684	-110.25764	1.00	2.00
44.320804	-110.269503	2.00	3.00
44.309417	-110.258012	1.00	2.00
44.327345	-110.269611	1.50	3.00
44.328479	-110.269803	1.50	3.00
44.339819	-110.2696	2.00	3.00

We again concentrated efforts on the West Thumb, but also flew Flat Mountain Arm and the Southern and Southeastern Arms. The data were presented as false-color images to identify groups of fish, and we created a table of fish locations. The fish hits are plotted in Figure 3.4a and listed in Table 3.1.

A second flight was undertaken during the 2016 lake trout spawning season on September 28. The flight altitude was again 300 meters, but this time the spot diameter was increased to five meters. For this flight we flew the entire shoreline of the lake, including the coastlines of all islands. Flight time was slightly over two hours. Data were again presented as false-color images. Figure 3.4b shows the fish hits we identified and Table 3.2 lists their locations.

Discussion

The 2004 flight yielded fish hits that correlated well with areas where fish had congregated during the spawning season, except in the northeastern and eastern part

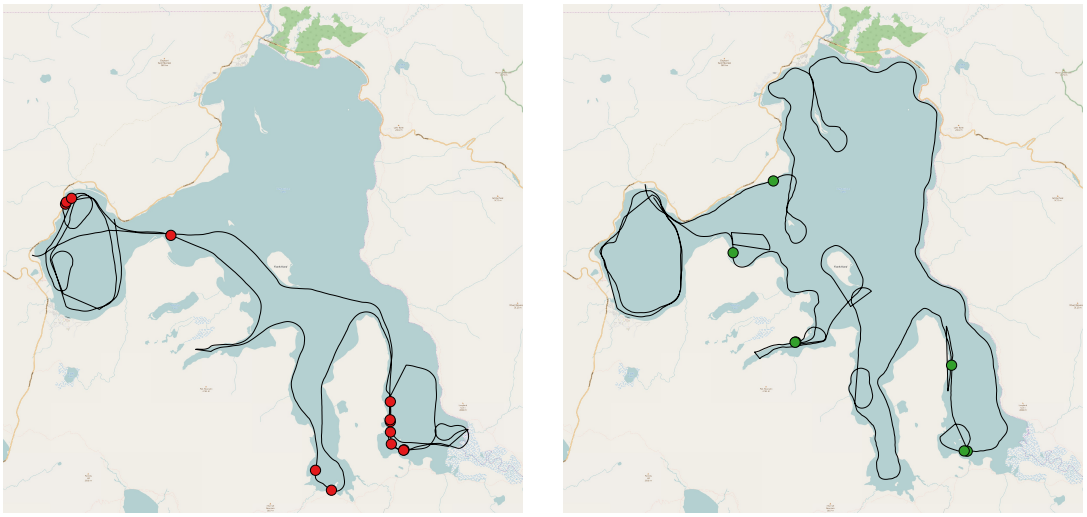

(a) (b)

Figure 3.4: Maps of fish hits identified from the lidar data in Yellowstone Lake from the 2015 and 2016 flights. The flight path taken each year is shown as a black line. 2015 fish hit data is shown in (a), with each hit identified as a red dot. We found several locations in the West Thumb, and the South and Southeast Arms. We did not fly the northeastern section of the lake as lake trout are not expected to be spawning in this part of the lake. 2016 fish hit data is shown in (b), with each location identified as a green dot. For this year we flew the coastline of the entire lake, including all the islands. We saw significantly fewer fish in 2016 than we did in 2015. The most fish activity was again seen in the southeastern arm. Top of the maps point north. Map data © OpenStreetMap contributors.

Table 3.2: Fish Hits – 2016

Latitude (°)	Longitude (°)	Fish Depth (m)	Bottom Depth (m)
44.432965	-110.459722	2.00	4.00
44.37717	-110.404897	1.50	2.00
44.376993	-110.405486	1.00	2.00
44.36262	-110.268539	1.00	2.50
44.30882	-110.254834	2.00	3.00
44.308999	-110.257472	1.00	2.00
44.477793	-110.424512	3.50	4.00

of the lake. We believe the backscatter signatures we saw in that area likely arose from bubbles coming from underwater thermal events that are common in that part of the lake. While it is not possible to definitively determine whether the locations identified in 2004, 2015, or 2016 were spawning sites, several of the areas found correspond with confirmed spawning sites.

Several studies have examined the depth of lake trout spawning sites. Claramunt evaluated egg mortality and predator densities at three different depths and concluded that lake trout preferred the shallowest depths as they increased egg survival [76]. However, shoals must also be deep enough to avoid freezing, and this limits the minimum depth at which trout may spawn [2, 76]. Bigelow reports it is unlikely that trout spawn in Yellowstone Lake below depths of 30 meters and success at sites greater than 10 meters is likely low [12]. Wind conditions during spawning season are also widely reported to play a strong role in selection of spawning sites [64–68], and it is thought that lake trout prefer spawning sites exposed to the prevailing wind, although this has been disputed [2]. Indeed, models of trout spawning sites in Yellowstone Lake predicted that they would occur primarily on the leeward side of land masses where they would be somewhat sheltered from the prevailing south-southwesterly winds during spawning season [12]. The data we recorded tends to agree with this theory since all identified groupings of fish occurred within close proximity of western, southwestern, and southern shores. Fish hits seen in the 2015 flight also correlated with National Park Service gillnet sets that were present on the same day.

Figure 3.5 shows an example fish hit from the 2015 data in the Southeast Arm of the lake, with the return from the fish indicated by an arrow. Each shot is adjusted for the vertical motion of the airplane by locating the surface return in the co-polarized channel and then aligned horizontally to create the image. One pixel in the image represents one sample from the data. During this flight the digitizers were operated

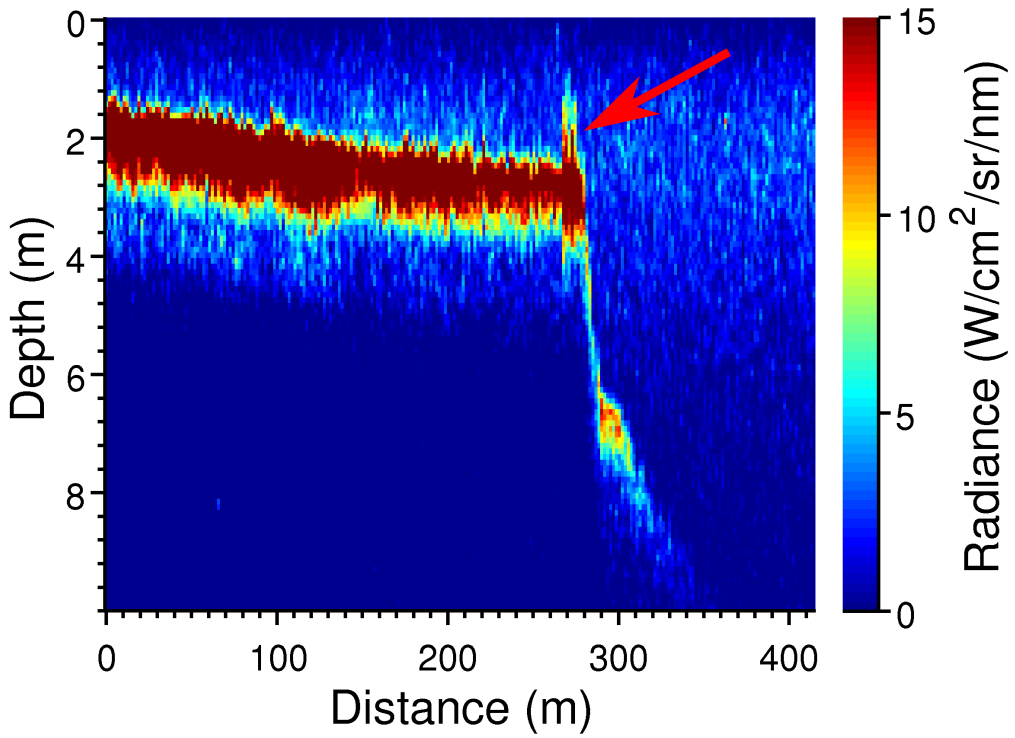

Figure 3.5: An example image from the 2015 flight, captured in the Southeast Arm of Yellowstone Lake. The red arrow points to the fish hit, which is the potential spawning site identified at 44.309684° N, 110.25764° W. These fish are immediately adjacent to the edge of an underwater drop-off which some authors have identified as a preferred structure for lake trout spawning sites [1, 2], though not all locations where we identified fish in Yellowstone Lake shared this pattern.

at 800 mega-samples per second; therefore each pixel represents roughly 14 cm of water depth.

The 2015 and 2016 flights were not exhaustive surveys of the lake, but were intended as a test of the lidar and technology. Currently our system uses a fixed beam, which limits the amount of water which can be surveyed. Several passes of an area must be performed for a complete survey. Many airborne lidars scan the beam along the transverse axis of the aircraft to increase the survey area. Our lidar did not

have that capability during this study; however, this is an improvement which would dramatically increase the efficiency of the system.

Conclusions

We found that airborne lidar can be successfully employed for searching and locating spawning sites for large-bodied fishes in large freshwater lakes. Indeed, lidar has several advantages over traditional, surface-based methods. Deployed from small aircraft, lidar instruments such as developed for this project are excellent for the specific mission of covering a spatially large survey area and can be deployed quickly and for comparatively low cost. Remote lakes that would be difficult to access from the ground can be easily mapped and studied within the span of a single day. It does not require invasive surgery to implant acoustic transmitters as with acoustic tracking, nor does it require expensive receivers with limited spatial coverage to be placed and maintained underwater.

While the species of fish detected cannot currently be determined from lidar data alone, useful information can be obtained when lidar data are combined with local knowledge of the lake and of the behavior of the species of interest. Areas with large groups of fish can be easily identified by examining the images produced from the data. While it is possible that the locations identified were areas where trout were feeding, identifying locations where fish congregate can help guide gill netting operations and locations which could be spawning sites. In this regard it can be used similarly to acoustic tracking devices, which are currently in use in Yellowstone and other area lakes to identify locations which could be spawning sites. When applied wisely, airborne lidar presents a promising tool for fisheries managers and researchers.

LIDAR ATTENUATION

The attenuation coefficient of lidar was first studied by Gordon in [24], where he derived a Monte Carlo simulation that included the effects of multiple scattering. He noted that the lidar attenuation coefficient α varied between the beam attenuation coefficient c and the diffuse attenuation coefficient of downwelling radiance K_d. For a narrow field-of-view (FOV) lidar, the attenuation coefficient is closer to the beam attenuation coefficient. As the FOV is broadened, the receiver will capture more multiply-scattered photons, and the attenuation coefficient approaches K_d. This is illustrated in the equation given by Churnside in [19], which was derived from Gordon's simulations and is reproduced below.

$$\alpha = K_d + (c - K_d)e^{-0.85cD}, \qquad \text{(2.2 revisited)}$$

where D is the lidar spot diameter on the water surface. As D increases, the quantity $(c - K_d)\exp(-0.85cD)$ grows smaller and the attenuation coefficient will approach K_d. Because K_d is typically much smaller than c it is important to use a wide FOV, as was shown in Chapter 2.

In [26] we simulated the performance of our lidar in Yellowstone Lake. To perform this simulation we were forced to derive estimates for c and K_d to compute α using Equation (2.2), as these data were unavailable for Yellowstone Lake. Also, the lidar attenuation coefficient is related to the water clarity, which is an important measurement with implications for recreation and habitat quality [77]. And as shown in Equation (2.2) it is also related to c and K_d. K_d in particular is a value which is strongly tied to important biological parameters, such as chlorophyll concentration [28, 51]. In this chapter we will compare our estimate for α to actual measurements of the attenuation coefficient taken in Yellowstone Lake in 2015 and 2016.

Method for Calculating the Attenuation Coefficient from Lidar Data

A program was developed to automate the computation of the lidar attenuation coefficient over entire datasets. Fundamentally, this program performs a non-linear least-squares fit on each shot to a model function

$$f(z) = ae^{-2bz}, \tag{4.1}$$

which is of the same form as Equation 2.1. $\beta(\pi, z)$ is assumed to be constant over depth, and the quantity $(nH + z)^2$ is also assumed to be approximately constant over the small range of depths considered. a and b are estimated; b is the lidar attenuation coefficient for that shot. As the lidar attenuation coefficient α is not polarization-dependent, the co- and cross-polarized signals were added together to form an un-polarized lidar signal.

The least-squares fit was not performed on all shots. Shots with a shallow lake bottom or the presence of fish or other targets were not suitable for attenuation coefficient calculation. The program discarded shots that fit several categories. First, any shot that was not monotonically decreasing within the depth range of interest was discarded. If the signal increased at any point more than 200% of the last decreasing value it was labeled invalid. This removed any shots with a significant bottom return. Second, each shot had to have a significant decline in radiance from the top depth to the bottom depth. For our calculations, this "significant decline" was set to be at least 5 $\mathrm{Wcm^{-2}sr^{-1}nm^{-1}}$. This removed shots which were mainly noise or where some other kind of error had occurred. Finally, any shot which was not a good fit to the model function, which was defined as any shot where the coefficient of determination for the fit $R^2 < 0.9$ or any shot where $b < 0$, was discarded.

Shots were also overlaid with a bathymetric map of Yellowstone Lake and any shot taken at a depth of less than 10 meters was removed.

Results for the 2015 and 2016 Flights

The program was run on the data from flights over Yellowstone Lake on 9 September 2015, 23 September 2015, 28 October 2015, and 28 September 2016. The 2015 flights utilized the narrow FOV receiver, where we would expect the lidar attenuation coefficient to more closely approximate the beam attenuation coefficient. The 2016 flight used the wide FOV receiver, and the attenuation coefficient should be closer to the diffuse attenuation coefficient.

In the simulation we calculated that for the narrow FOV case $\alpha = 0.4579$, and for the wide FOV case $\alpha = 0.2630$. Flight altitude was assumed to be 300 m, other parameters were the same as in [26].

Wide FOV

The only wide FOV flight of Yellowstone Lake occurred on September 28, 2016. The software was set to compute the attenuation coefficient from 4 to 10 m in depth. We removed outliers with $\alpha > 0.75$ as these were obviously erroneous. Figure 4.1 displays a histogram of the attenuation data. We noted that the distribution is strongly right-skewed with a median of 0.2603 m^{-1}, a mean of 0.3102 m^{-1}, and a spatial standard deviation of 0.1037 m^{-1}. The mean root-mean-square error (RMSE) of the residuals of α was 0.006 (computed as the root-mean-square deviation of the data points from the model function).

In simulation the calculated attenuation coefficient was 0.2630, which falls within one standard deviation of the measured attenuation coefficient and is nearly identical

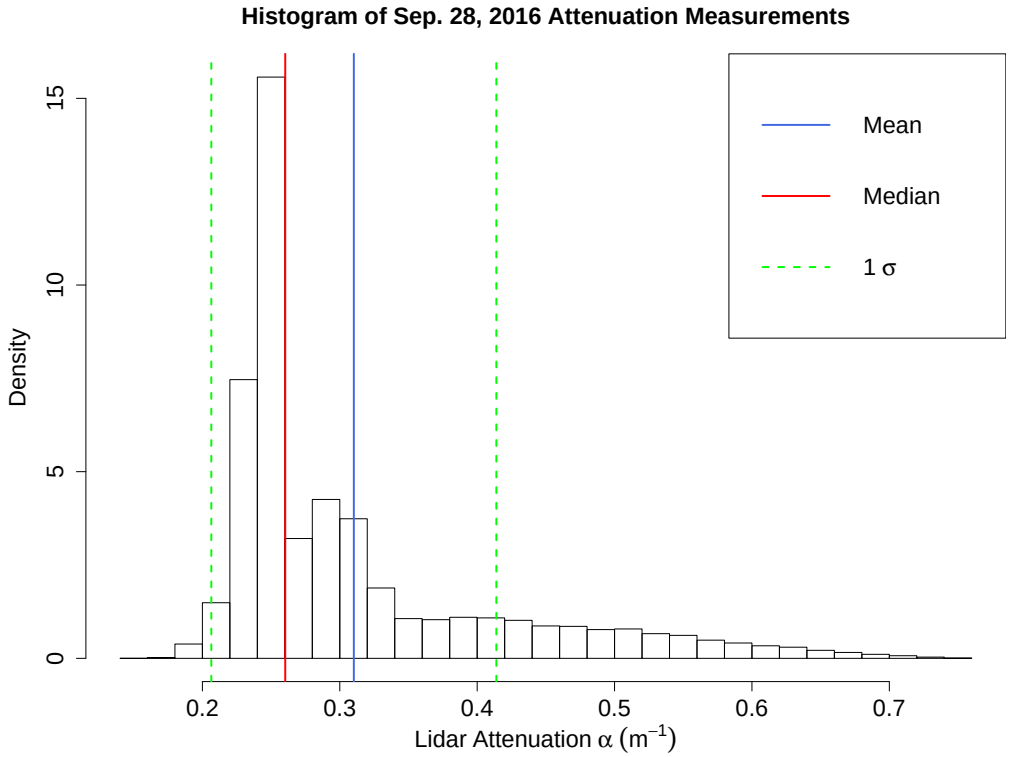

Figure 4.1: A histogram of the September 28, 2016 attenuation data. The mean was 0.3102 m^{-1}, the median was 0.2603 m^{-1}, and standard deviation was 0.1037 m^{-1}.

to the median value. This modeled value then appears reasonable, although the data are still highly skewed.

The data were sampled every 100th point and tested using Moran's I in R [78,79] for spatial autocorrelation. Weights were the inverse Euclidean distance between points. The calculated value, $I = 0.41$ was evidence for positive autocorrelation. Significance was tested against a null distribution obtained by calculating Moran's I for 1000 random permutations of the data, and the null hypothesis of no spatial correlation was rejected at the 5% significance level ($p = 0$, sd $= 0.0058$). This result would be expected: neighboring parts of the lake should have similar light attenuation values.

Next we were interested in visualizing how the attenuation coefficient changed as one moved farther away from a given point in the lake. To assess this we created a variogram using the rgdal and geoR packages in R [80,81], which displays the variance versus distance. The variance $\hat{\gamma}(h)$ is defined as

$$\hat{\gamma}(h) = \frac{1}{2N(h)} \sum_{i=0}^{N(h)} \left[\alpha(\mathbf{x}_i) - \alpha(\mathbf{x}_i + \mathbf{h})\right]^2 \tag{4.2}$$

where $\alpha(\mathbf{x})$ is the attenuation measured at $\mathbf{x}$, $h = \|\mathbf{h}\|$, and $N(h)$ is the number of data pairs separated by a distance h [82]. The variogram, then, is a plot of the estimated variance at a given separating distance h between attenuation measurements. It allows us to assess how the attenuation coefficient changes over the lake, and how uniform the attenuation over the lake is. Figure 4.2 displays the variogram calculated for the data.

Figure 4.3 is a map of the attenuation data. We noted the concentration of high attenuation value in the South Arm. This may be because of the inlet of the Yellowstone River being located at the southern end of the South Arm, which would increase the amount of mixing and thus the concentration of dissolved organic matter in those waters. High attenuation values were not noted in the remainder of the lake except at sporadic points which may indicate a shallow lake bottom being present which was not caught by the software or the previous analyses or perhaps an in-water plume.

Narrow FOV

Three flights were undertaken on September 9, 23, and October 28, 2015 with the narrow FOV configuration. Data points close to shore were again excluded from the analysis, as were data points with $\alpha > 1$, as these points were obviously incorrect and

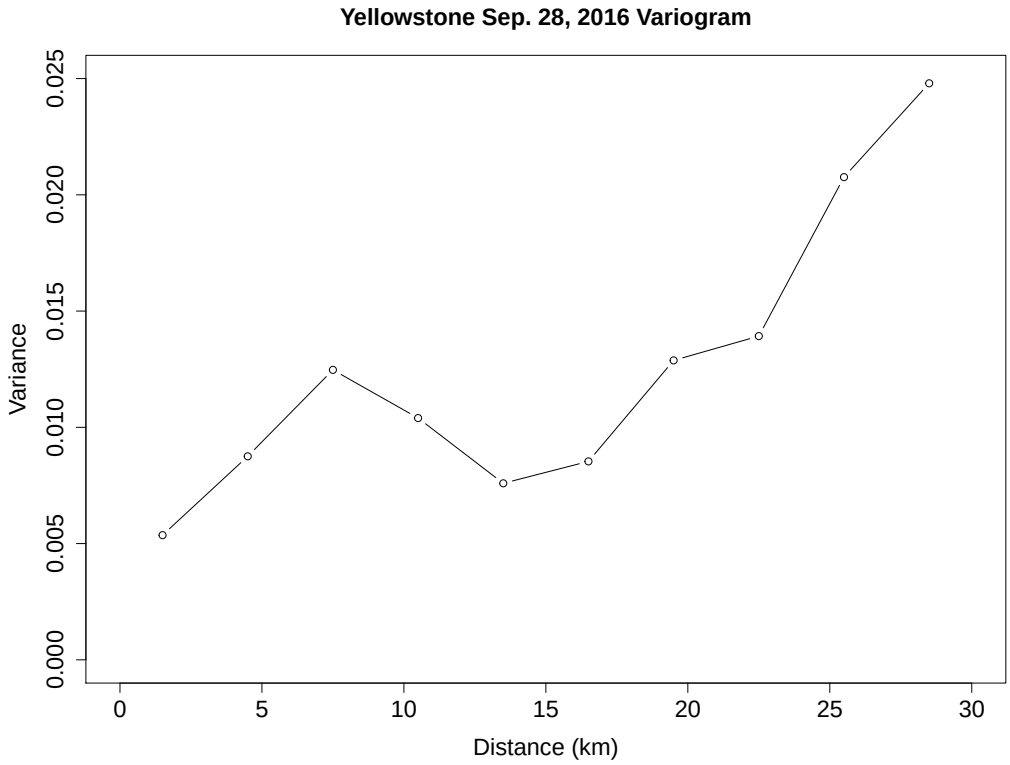

Figure 4.2: The variogram calculated for the September 28, 2016 lidar attenuation data.

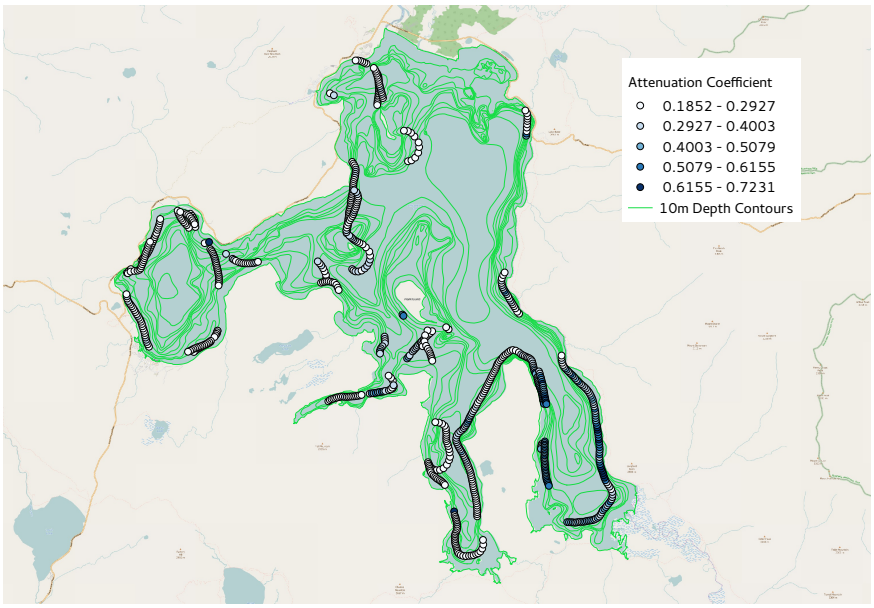

Figure 4.3: A map of the attenuation coefficients from the 2016/09/28 flight.

accounted for less than 0.3% of each dataset. For this configuration the attenuation was calculated between 2 and 5 meters in depth because of the smaller penetration depth.

The data were again sampled every 100th point and tested for spatial autocorrelation using Moran's I. The null hypothesis of no autocorrelation was rejected in all cases at the 5% significance level (September 9, $I = 0.144$, $p = 0$, sd $= 0.0081$; September 23, $I = 0.219$, $p = 0$, sd $= 0.0089$; October 28, $I = 0.1440$, $p = 0$, sd $= 0.0092$).

For September 9 the mean was 0.6806, the median was 0.7243, and the spatial standard deviation was 0.1460. The mean RMSE of the residuals of α was 0.03 (calculated the same as for the wide FOV). Figure 4.4 shows a histogram of the data and Figure 4.8 is a map of the data. For September 23 the mean was 0.4123, the median was 0.3076, and the spatial standard deviation was 0.2012. The mean RMSE of the residuals of α was 0.017. Figure 4.5 shows a histogram of the data and Figure 4.9 is a map of the data. For October 28 the mean was 0.6581, the median was 0.6885, and the spatial standard deviation was 0.1301. The mean RMSE of the residuals of α was 0.037. Figure 4.6 shows a histogram of the data and Figure 4.10 is a map of the data.

On September 9, the attenuation over the lake was fairly uniform. However, near the outlet of the Yellowstone River the attenuation became much lower. It is possible that the river water clarity is greater than that of the lake, which would explain this effect. On September 23, the outlet of the river also showed less attenuation than in other areas of the lake.

On September 23, the simulated attenuation fell within one standard deviation of the measured mean, but the measured mean on the other two flights was higher than simulation. Significant wildfire smoke was present in the weeks preceding the

September 9 flight, and more plankton would have been present during this time than the later flights, which all could have increased the attenuation of the water. Fall typically sees a decline in phytoplankton in temperate, dimictic lakes [83], which is reflected in temporal samples of plankton from Yellowstone Lake [49]. Prior to the October 28 flight there was rain over the previous three days which would increase the turbidity of the water, and during the flight a 1.75 m/s wind was present over the lake, which would increase mixing near the surface and also increase the turbidity.

On October 28, the attenuation was higher, with areas of lower attenuation mixed with areas of higher attenuation in no discernible pattern.

Figure 4.7 displays the variogram for the 2015 data. While the attenuation coefficient standard deviation remains similar for each flight, the variogram shows some remarkable differences. On September 9, the lake was fairly uniform, with the variance not increasing above 0.02 m until about 20 km. On September 23, the variance had increased significantly, although the lake was still fairly uniform. The variance had decreased on October 28, and it remains at or below 0.02 m throughout the survey area. Yellowstone Lake is dimictic, and by this point the lake should have turned over and become completely mixed [84]. Lakes can thermally stratify, wherein they develop defined thermal layers. A lakes "mixes" or "turns over" when these layers disappear and the temperature is uniform from the surface to the bottom. In a dimictic lake this occurs twice per year, generally in spring and fall.

Conclusion

For the one flight in 2016, the simulated attenuation value was within one standard deviation of the mean measured attenuation value. In 2015 this only occurred on one out of three flights. The attenuation coefficient does not appear to be uniform over the entire lake. Instead, the attenuation coefficient appears to be

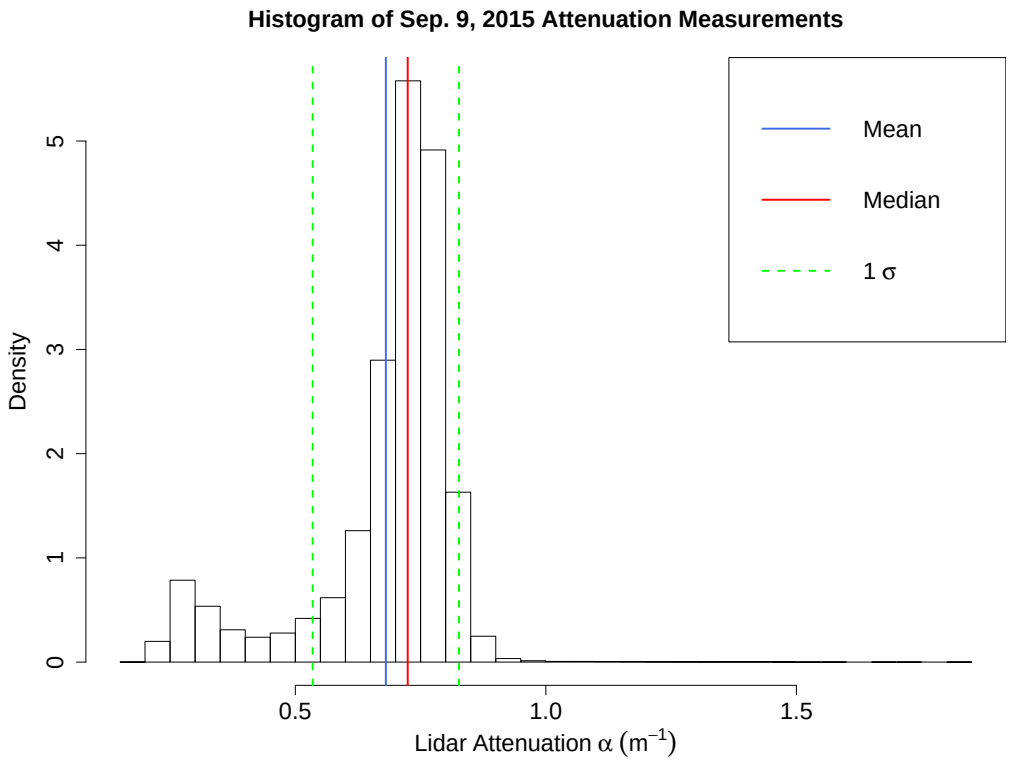

Figure 4.4: Histogram of the 2015/09/09 attenuation data.

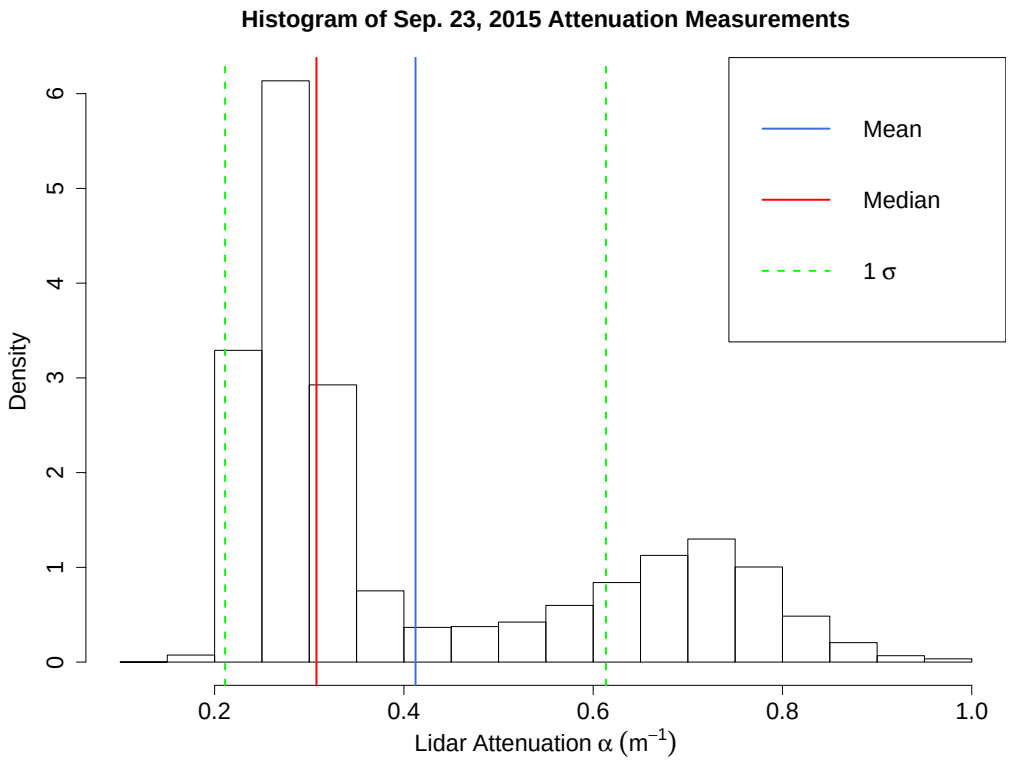

Figure 4.5: Histogram of the 2015/09/23 attenuation data.

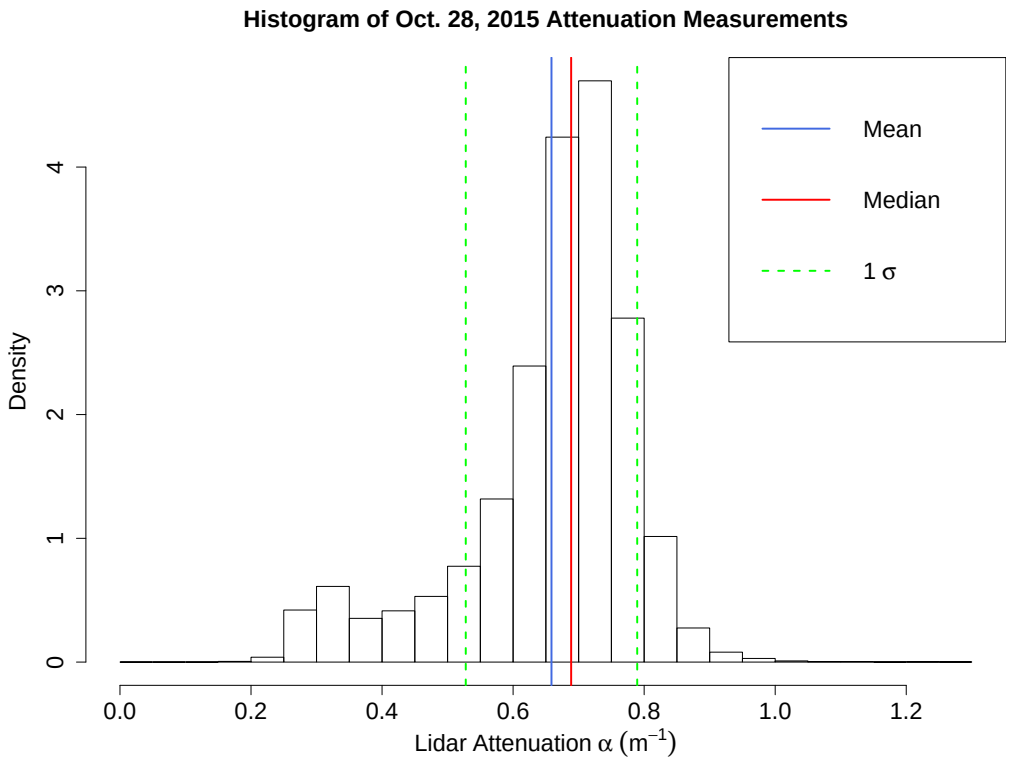

Figure 4.6: Histogram of the 2015/10/28 attenuation data.

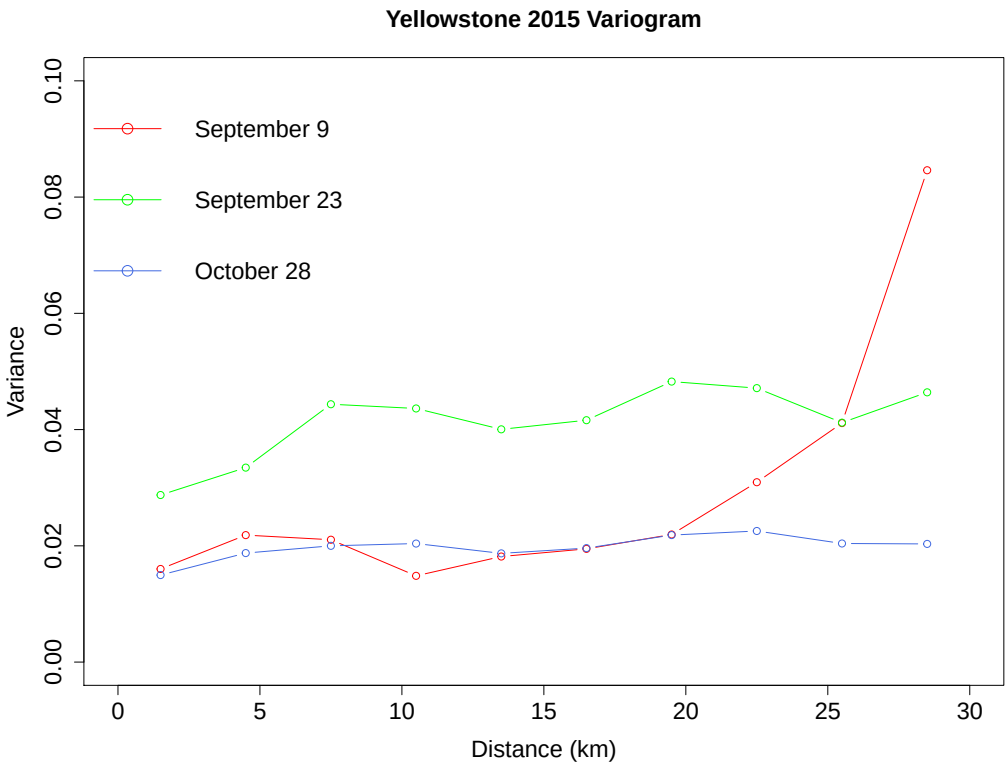

Figure 4.7: Variogram of the 2015 attenuation data.

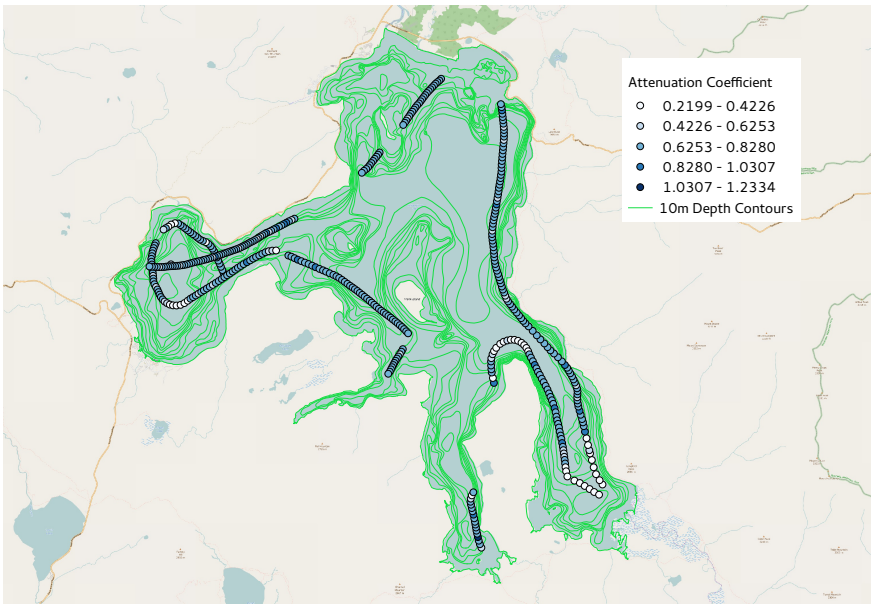

Figure 4.8: Map of the 2015/09/09 attenuation data.

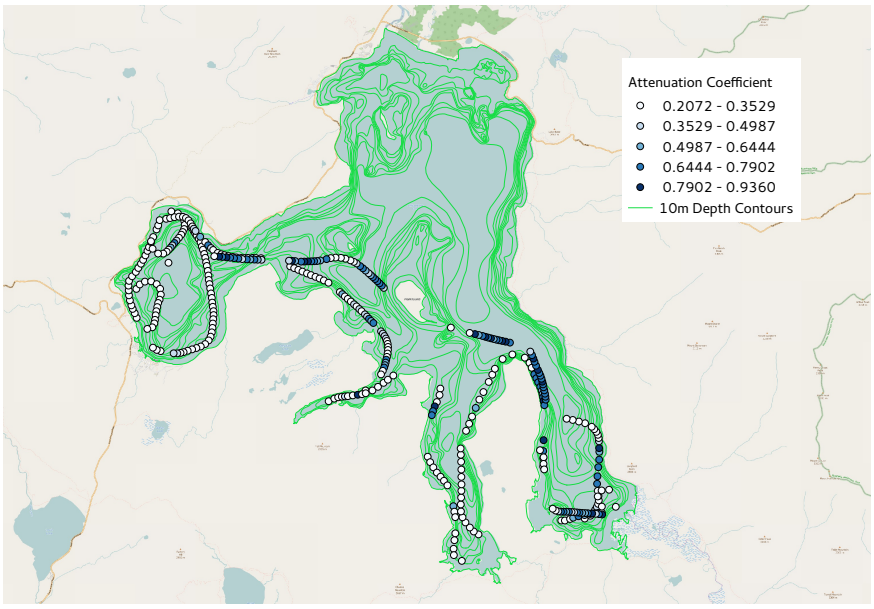

Figure 4.9: Map of the 2015/09/23 attenuation data.

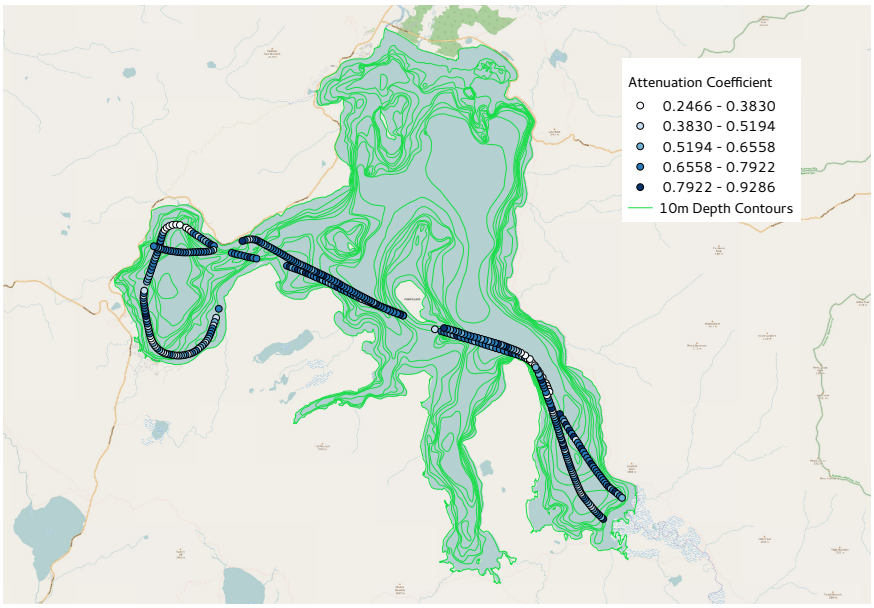

Figure 4.10: Map of the 2015/10/28 attenuation data.

localized, and different parts of the lake may have significantly different attenuation coefficients. It also appears to depend on recent weather and other atmospheric conditions. Further investigation is needed to quantify how different conditions affect the attenuation coefficient at different times of the year.

LIDAR DETECTION OF UNDERWATER THERMAL VENTS

In this chapter we report the suspected detection of underwater thermal vents in Yellowstone Lake with lidar, captured during the September 28, 2016 flight. To our knowledge, this has not been previously reported in the literature. Figure 5.1 shows a lidar image of a suspected thermal vent. The location was at 44.424745° N, 110.571984° W. There appears to be a plume above the vent near surface. Figure 5.2 is a picture of the area where the vent was identified taken from the plane. The reddish-brown color of the bottom near this area could be from iron-oxide, which is commonly deposited by sublacustrine thermal vents in Yellowstone Lake [3]. The dome-shaped structure has been reported by others as a characteristic of some hydrothermal vents in Yellowstone Lake [29, 33].

There are several possible explanations for the plume. Hydrothermal vents commonly release large volumes of sediment [3], and this entrained sediment may cause the higher lidar return. The warmer water may support a plankton layer which would create a higher return also. Bubbles are also commonly present, which would also create a higher return [29].

Figure 5.3 shows a map of thermal vents from a 2007 survey performed by Shanks et al. [3] and the thermal vent discussed above. The nearest vent location reported by Shanks is only 30 meters away, which is a very reasonable error given that the tilt of the plane is not currently accounted for when computing a shot location, and the GPS unit is often only accurate to 10 meters.

Figure 5.4 shows another lidar image of a second suspected thermal vent at 44.477793° N, 110.424512° W. The lidar data show the same pattern as the first thermal vent, however, the USGS did not report any thermal vents within 2 km of its location. Figure 5.5 shows a picture of this vent taken from the plane. The

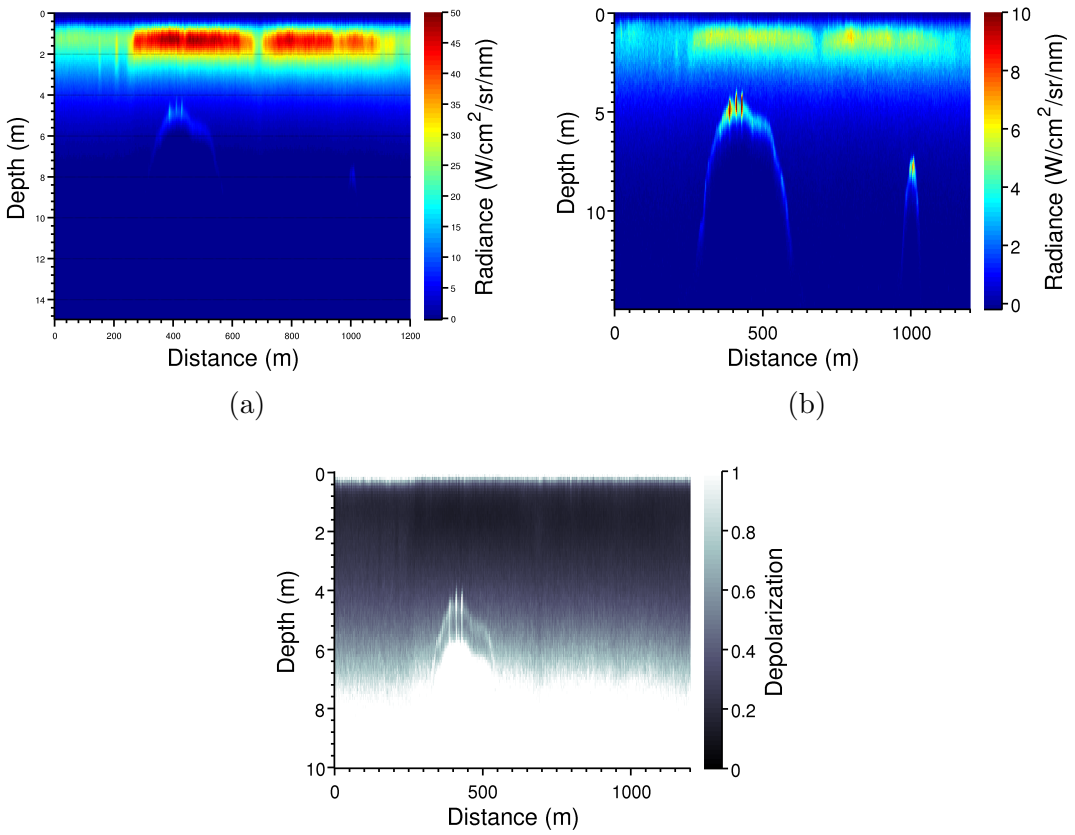

Figure 5.1: Lidar image from the (a) co-polarized channel, (b) cross-polarized channel, and (c) depolarization image of a suspected underwater thermal vent in Yellowstone Lake at the West Thumb Geyser Basin. Note that the scales are not equivalent for each channel.



Figure 5.2: A picture taken from the plane of the thermal vent identified in Figure 5.1. The reddish-brown color could be from iron-oxide, which is common near thermal vents in Yellowstone Lake [3].

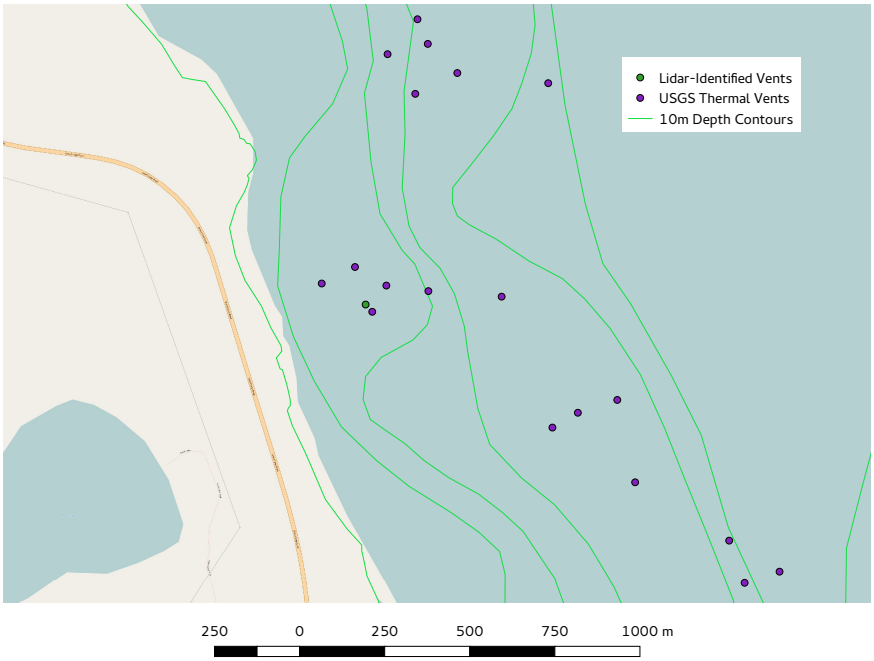

Figure 5.3: A map showing USGS-identified thermal vents and the location of the vent shown in Figure 5.1. The nearest USGS-identified thermal vent is 30 meters away. Top of the maps point north. USGS thermal vent and bathymetry data from [4]. Base map data © OpenStreetMap contributors.

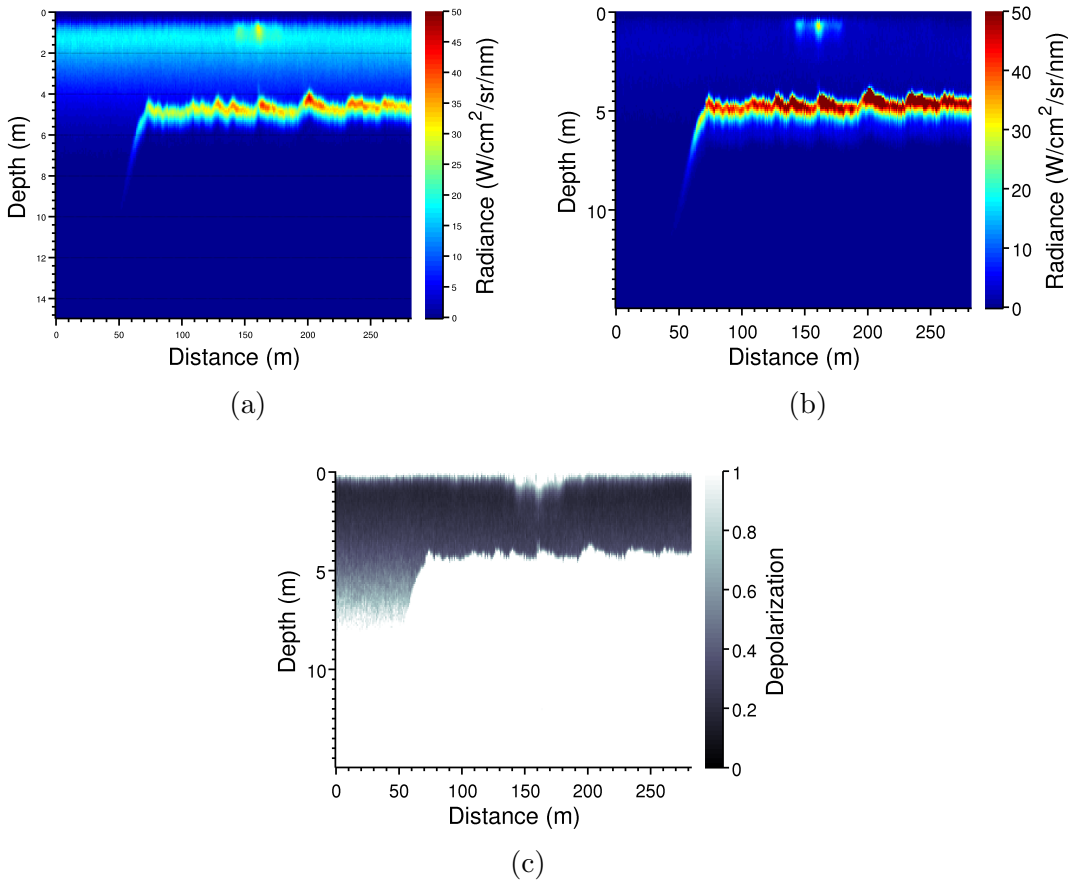

Figure 5.4: Lidar image from the (a) co-polarized channel, (b) cross-polarized channel, and (c) depolarization image of a second suspected thermal vent. This image shows the same pattern as the first thermal vent from Figure 5.1, but the USGS did not identify any thermal vents near its location.

bottom is again reddish-brown. Figure 5.6 shows the location of this possible thermal vent in relation to the Shanks-identified thermal vents, and Figure 5.7 is an overview map showing the locations of both thermal vents in relation to the USGS-identified thermal vents.



Figure 5.5: A picture taken from the plane of the second suspected thermal vent shown in Figure 5.4. The lake bottom is again reddish-brown, which is a common characteristic of thermal vents in Yellowstone Lake.

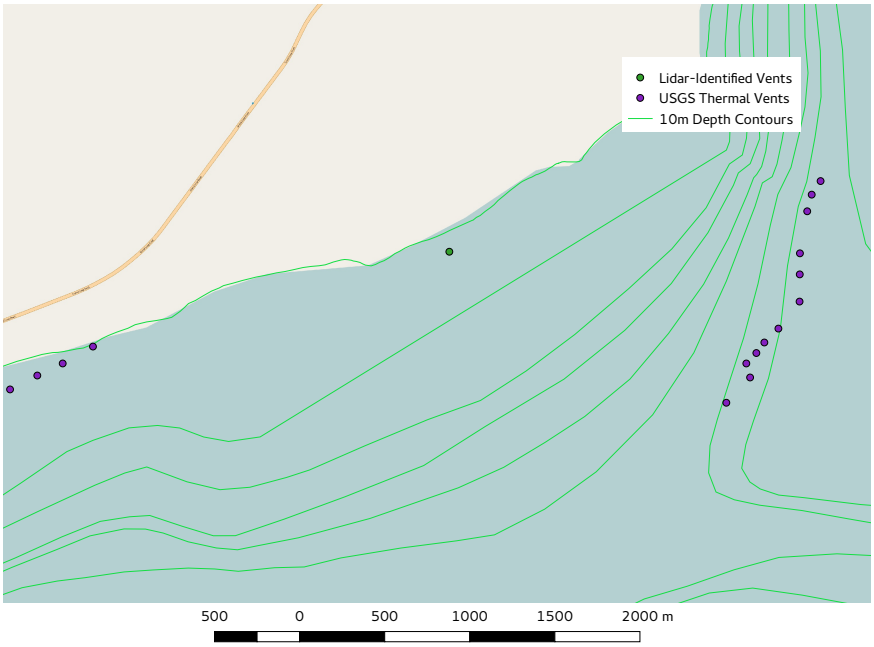

Figure 5.6: A map showing USGS-identified thermal vents and the location of the vent shown in Figure 5.4. The nearest USGS-identified thermal vent is over 2 km away. Top of the maps point north. USGS thermal vent and bathymetry data from [4]. Base map data © OpenStreetMap contributors.

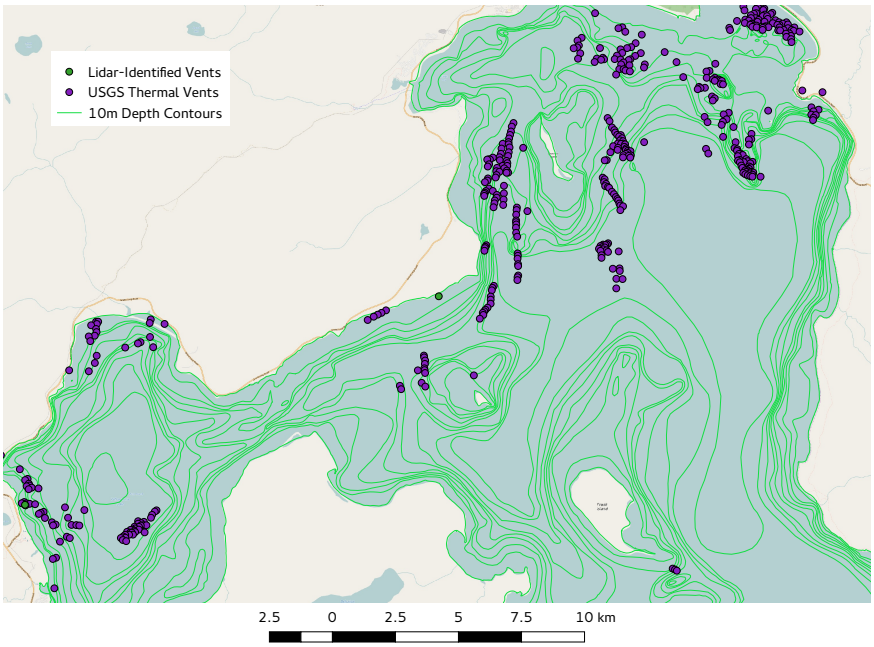

Figure 5.7: An overview map showing the USGS-identified thermal vents in relation to the lidar-identified thermal vents. Top of the map points north. USGS thermal vent and bathymetry data from [4]. Base map data © OpenStreetMap contributors.

Discussion and Conclusion

We are not aware of any prior work discussing the detection of sublacustrine thermal vents with lidar. The correlation of the first possible vent's location with the Shanks vent data, the coloration of the lake bottom, and the domed structure are strong evidence that this is indeed a thermal vent. While Shanks did not indicate that a thermal vent existed at the location of the second possible vent, the data appeared similarly to the first with the existence of a plume just below the surface, and a smaller jet appearing on the lake bottom. This possible vent was not dome-shaped like the previous case.

It is also possible that the jets are not jets at all, but instead "underwater chimneys" created by the thermal vent. Morgan and Remsen report the existence of underwater chimneys from thermal vents, but there is disagreement in the literature on whether these are active. Remsen reports active underwater thermal chimneys, several meters in length and between 10- and 20-cm in diameter [29, 31]. Morgan reports the existence of chimneys but also states that none of these chimneys are currently known to be active [33].

It is clear that further investigation is needed. Are these indeed thermal vents? What creates the surface plume? Is it sediment, plankton, bubbles, or something else? If it is sediment or bubbles, why do we not see a brighter return between the layer and the vent? What causes the bright, jet-like returns to appear at the location of the vent? Ideally, a lidar flight would coincide with surface observations. Hopefully this is work that can be performed in the future.

DISCUSSION OF FRESHWATER AIRBORNE LIDAR AND FUTURE WORK

In this dissertation we have presented the design of and several uses of airborne lidar for studying freshwater ecosystems. Numerous studies have examined airborne lidar in saltwater, and while far less research exists in freshwater, the design of the lidar remains largely the same. Freshwater does have some differences, with a typically higher chlorophyll and dissolved organic matter concentration that limits penetration depth, and the depth of study is often not as great.

Airborne lidar shows promise for performing freshwater fisheries surveys. While it cannot currently identify the species of fish seen, it is capable of identifying groupings of fish and their depth and the depth to the bottom. This is often enough information for biologists to make an informed guess as to the species of the fish. For identifying the spawning sites of lake trout airborne lidar can be used similarly to acoustic tagging, where trout are implanted with acoustic pingers which allows their location to be tracked when they are near submerged receivers. These data are used to identify potential spawning sites by noting where fish are repeatedly congregating and then considering the depth of the water and the depth of the fish, the same as with airborne lidar.

More study is needed with better "ground-truthing," with airborne measurements of fish being corroborated with surface measurements. The measurement of the optical properties of freshwater fish would also be useful, and would hopefully allow for lidar-based estimates of biomass. Studies of other lakes would be important as well. During the course of our work we flew Flathead Lake during its lake trout spawning season but were unable to locate any fish. It would be important to verify that this method is applicable outside of Yellowstone.

Measurements of the lidar attenuation coefficient can also be extracted from lidar data. This coefficient has a qualitative relationship with the beam attenuation coefficient and the coefficient of downwelling radiance, and with further work it may be possible to extract these coefficients from lidar measurements. Currently the only optical study of many lakes is repeated Secchi disk samplings, which at best are done at a handful of locations. The literature is rife with articles discussing the severe limitations of the Secchi disk, but because of its low cost and simple application it is still widely used. Airborne lidar could provide optical measurements which are less subjective and over a larger area. Also, we are not aware of any studies that have examined the spatial heterogeneity of lake optical properties (with Secchi disk measurements or otherwise), and this is another area of potential application for airborne lidar.

Ground-truthing is again the next important step for measuring the attenuation coefficient. Comparison with transmissometer measurements would be a logical next step. If a relationship can be established the lidar data would have much more utility, and knowledge of how optical properties vary spatially could have a significant impact on our understanding of lakes.

Lidar study of thermal vents is also a novel application. Significant research is needed to verify the measurements we made and to determine the utility of lidar measurements.

Airborne lidar's advantage over other methods often lies in its ability to quickly survey great distances, and the ease at which remote areas can be accessed. Many biological measurements are currently surface-based and are limited in their spatial coverage (the notable exception, of course, being satellite measurements, which are limited in their resolution). These measurements are expensive and time-consuming, especially if the lake to be measured is remote or large. While surface measurements

are typically more detailed than what can be done with airborne lidar, taking surface measurements over the same distance and resolution as a lidar study is completely impractical. Airborne lidar will never replace surface measurements, but it has the potential to greatly improve our understanding of how processes and species vary spatially over large and remote lakes.

REFERENCES CITED

[1] Stephen C. Riley, Thomas R. Binder, Nigel J. Wattrus, Matthew D. Faust, John Janssen, John Menzies, J. Ellen Marsden, Mark P. Ebener, Charles R. Bronte, Ji X. He, et al. Lake trout in northern lake huron spawn on submerged drumlins. *Journal of Great Lakes Research*, 40(2):415–420, 2014.

[2] David T. Callaghan, Paul J. Blanchfield, and Peter A. Cott. Lake trout (salvelinus namaycush) spawning habitat in a northern lake: The role of wind and physical characteristics on habitat quality. *Journal Of Great Lakes Research*, 42:299–307, 2016.

[3] Lisa A. Morgan, editor. *Integrated Geoscience Studies in the Greater Yellowstone Area-Volcanic, Tectonic, and Hydrothermal Processes in the Yellowstone Geoecosystem*, chapter G. Number 1717. US Geological Survey, 2007.

[4] L. A. Morgan, Wayne C. Shanks, G. K. Lee, and M. W. Webring. Bathymetry and geology of the floor of yellowstone lake, yellowstone national park, wyoming, idaho, and montana. Technical report, US Geological Survey, 2007. Scientific Investigations Map 2973.

[5] Todd M. Koel, Patricia E. Bigelow, Philip D. Doepke, Brian D. Ertel, and Daniel L. Mahony. Conserving yellowstone cutthroat trout for the future of the gye. *Yellowstone Science*, 14(2):20–28, 2006.

[6] Lynn R. Kaeding, Glenn D. Boltz, and Daniel G. Carty. Lake trout discovered in yellowstone lake threaten native cutthroat trout. *Fisheries*, 21(3):16–20, 1996.

[7] Andrew R. Munro, Thomas E. McMahon, and James R. Ruzycki. Natural chemical markers identify source and date of introduction of an exotic species: lake trout (salvelinus namaycush) in yellowstone lake. *Canadian Journal of Fisheries and Aquatic Sciences*, 62(1):79–87, 2005.

[8] Todd M. Koel, Patricia E. Bigelow, Philip D. Doepke, Brian D. Ertel, and Daniel L. Mahony. Nonnative lake trout result in yellowstone cutthroat trout decline and impacts to bears and anglers. *Fisheries*, 30(11):10–19, 2005.

[9] John M. Syslo, Christopher S. Guy, Patricia E. Bigelow, Philip D. Doepke, Brian D. Ertel, and Todd M. Koel. Response of non-native lake trout (salvelinus namaycush) to 15 years of harvest in yellowstone lake, yellowstone national park. *Canadian Journal of Fisheries and Aquatic Sciences*, 68(12):2132–2145, 2011.

[10] Robert E. Gresswell, Cory D. Suski, Michael Parsley, Todd Koel, Patricia E. Bigelow, Brian D. Ertel, Andy J. Danylchuk, and Steven J. Cooke. Identifying movement patterns and spawning areas of invasive lake trout salvelinus namaycush in yellowstone lake. Technical report, US Geological Survey, Northern Rocky Mountain Science Center, Bozeman, MT 59715, April 2012.

[11] Patrick J. Martinez, Patricia E. Bigelow, Mark A. Deleray, Wade A. Fredenberg, Barry S. Hansen, Ned J. Horner, Stafford K. Lehr, Roger W. Schneidervin, Scott A. Tolentino, and Art E. Viola. Western lake trout woes. *Fisheries*, 34(9):424–442, 2009.

[12] Patricia Ellen Bigelow. *Predicting areas of lake trout spawning habitat within Yellowstone Lake, Wyoming*. PhD thesis, University of Wyoming, 2009.

[13] Benjamin Samuel Cox. Assessment of an invasive lake trout population in swan lake, montana. Master's thesis, Montana State University-Bozeman, College of Letters & Science, 2010.

[14] David L. Murphree, Clayborne D. Taylor, and Ronald W. McClendoni. Mathematical modeling for the detection of fish by an airborne laser. *AIAA Journal*, 12(12):1686–1692, 1974.

[15] James L. Squire and Howard Krumboltz. Profiling pelagic fish schools using airborne optical lasers and other remote sensing techniques. *Mar. Technol. Soc. J*, 15:27–31, 1981.

[16] Margarita M. Krekova, Georgiy M. Krekov, Ignatiy V. Samokhvalov, and Vitaliy S. Shamanaev. Numerical evaluation of the possibilities of remote laser sensing of fish schools. *Applied optics*, 33(24):5715–5720, 1994.

[17] R. W. Gauldie, S. K. Sharma, and C. E. Helsley. Lidar applications to fisheries monitoring problems. *Canadian Journal of Fisheries and Aquatic Sciences*, 53(6):1459–1468, 1996.

[18] James H. Churnside, Viatcheslav V. Tatarskii, and James J. Wilson. Airborne lidar for fisheries applications. *Optical Engineering*, 40(3):406–414, 2001.

[19] James H. Churnside. Review of profiling oceanographic lidar. *Optical Engineering*, 53(5), 2014.

[20] James H. Churnside, David A. Demer, and Behzad Mahmoudi. A comparison of lidar and echosounder measurements of fish schools in the gulf of mexico. *ICES Journal of Marine Science: Journal du Conseil*, 60(1):147–154, 2003.

[21] James H. Churnside, David A. Demer, David Griffith, Robert L. Emmett, and Richard Brodeur. Comparisons of lidar, acoustic and trawl data on two scales in the northeast pacific ocean. *CalCOFI Rep*, 50:118–122, 2009.

[22] James H. Churnside and Philip A. McGillivary. Optical properties of several pacific fishes. *Applied optics*, 30(21):2925–2927, 1991.

[23] James H. Churnside, James J. Wilson, and Viatcheslav V. Tatarskii. Lidar profiles of fish schools. *Applied Optics*, 36(24):6011–6020, 1997.

[24] Howard R. Gordon. Interpretation of airborne oceanic lidar: effects of multiple scattering. *Applied optics*, 21(16):2996–3001, 1982.

[25] James H. Churnside, Viatcheslav V. Tatarskii, and James J. Wilson. Oceanographic lidar attenuation coefficients and signal fluctuations measured from a ship in the southern california bight. *Applied optics*, 37(15):3105–3112, 1998.

[26] Michael R. Roddewig, Nathan J. Pust, James H. Churnside, and Joseph A. Shaw. Dual-polarization airborne lidar for freshwater fisheries management and research. *Optical Engineering*, 56(3):031221, 2017.

[27] E. Ann Gallie and P. A. Murtha. Specific absorption and backscattering spectra for suspended minerals and chlorophyll-a in chilko lake, british columbia. *Remote Sensing of Environment*, 39(2):103–118, 1992.

[28] John T.O. Kirk. *Light and photosynthesis in aquatic ecosystems*. Cambridge university press, Cambridge, UK, 1994.

[29] Charles C. Remsen, James S. Maki, J. Val Klump, Carmen Aguilar, Patrick D. Anderson, Lorie Buchholz, Russell L. Cuhel, David Lovalvo, Robert W. Paddock, James Waples, et al. Sublacustrine geothermal activity in yellowstone lake: studies past and present. In *Yellowstone Lake: Hotbed of chaos or reservoir of resilience*, pages 192–212, 2002.

[30] J. V. Klump, C. C. Remsen, and J. L. Kaster. The presence and potential impact of geothermal activity on the chemistry and biology of yellowstone lake, wyoming. *Global Venting, Midwater and Benthic Ecological Processes*, (88-4):81–98, 1988.

[31] C. C. Remsen, J. Val Klump, J. Kaster, R. Paddock, P. Anderson, and J. S. Maki. Hydrothermal springs and gas fumaroles in yellowstone lake, yellowstone national park, wyoming. *National Geographic Research*, 6(4):509–515, 1990.

[32] L. A. Buchholz, P. D. Anderson, R. L. Cuhel, J. V. Klump, J. E. Kostka, R. W. Paddock, C. C. Remsen, J. S. Maki, and D. Lovalvo. Employment of rov techniques and scuba in yellowstone lake. In *Diving for science...1995: proceedings of the American Academy of Underwater Sciences Fifteenth Annual Scientific Diving Symposium*. American Academy of Underwater Sciences, 1995.

[33] L. A. Morgan, W. C. Shanks, D. A. Lovalvo, S. Y. Johnson, W. J. Stephenson, K. L. Pierce, S. S. Harlan, C. A. Finn, G. Lee, M. Webring, B. Schulze, J. Dühn, R. Sweeney, and L. Balistrieri. Exploration and discovery in yellowstone lake: results from high-resolution sonar imaging, seismic reflection profiling, and submersible studies. *Journal of Volcanology and Geothermal Research*, 122:221–242, apr 2003.

[34] Laurie S. Balistrieri, Wayne C. Shanks III, Russell L. Cuhel, Carmen Aguilar, and J. Val Klump. The influence of sublacustrine hydrothermal vent fluids on the geochemistry of yellowstone lake. Technical report, United States Geological Survey, 2007.

[35] Tingting Yang, Shawn Lyons, Carmen Aguilar, Russell Cuhel, and Andreas Teske. Microbial communities and chemosynthesis in yellowstone lake sublacustrine hydrothermal vent waters. *Front Microbiol*, 2:130, 2011.

[36] Frank E. Hoge, C. Wayne Wright, William B. Krabill, Rodney R. Buntzen, Gary D. Gilbert, Robert N. Swift, James K. Yungel, and Richard E. Berry. Airborne lidar detection of subsurface oceanic scattering layers. *Applied optics*, 27(19):3969–3977, 1988.

[37] O. A. Bukin, A. Yu Major, A. N. Pavlov, B. M. Shevtsov, and E. D. Kholodkevich. Measurement of the lightscattering layers structure and detection of the dynamic processes in the upper ocean layer by shipborne lidar. *International Journal of Remote Sensing*, 19(4):707–715, 1998.

[38] Alexander P. Vasilkov, Yury A. Goldin, Boris A. Gureev, Frank E. Hoge, Robert N. Swift, and C. Wayne Wright. Airborne polarized lidar detection of scattering layers in the ocean. *Applied optics*, 40(24):4353–4364, 2001.

[39] Gary C. Guenther. Airborne laser hydrography: System design and performance factors. Technical report, DTIC, Fort Belvoir, VA, 1985.

[40] Gary C. Guenther. Wind and nadir angle effects on airborne lidar water surface returns. In *1986 Technical Symposium Southeast*, pages 277–286, 1986.

[41] Gary C. Guenther, Robert WL Thomas, and Paul E. LaRocque. Design considerations for achieving high accuracy with the shoals bathymetric lidar system. In *CIS Selected Papers: Laser Remote Sensing of Natural Waters–From Theory to Practice*, pages 54–71, 1996.

[42] James H. Churnside, Kouichi Sawada, and Tsuyoshi Okumura. A comparison of airborne lidar and echo sounder performance in fisheries. *Journal of the Marine Acoustic Society of Japan*, 28(3):175–187, 2001.

[43] J. H. Churnside and L. A. Ostrovsky. Lidar observation of a strongly nonlinear internal wave train in the gulf of alaska. *International Journal of Remote Sensing, vol. 26, issue 1, pp. 167-177*, 26:167–177, jan 2005.

[44] James H. Churnside. Lidar signature from bubbles in the sea. *Optics express*, 18(8):8294–8299, 2010.

[45] James H. Churnside, Richard D. Marchbanks, Jennifer H. Lee, Joseph A. Shaw, Alan Weidemann, and Percy L. Donaghay. Airborne lidar detection and characterization of internal waves in a shallow fjord. *Journal of Applied Remote Sensing*, 6(1), 2012.

[46] James H. Churnside and Percy L. Donaghay. Thin scattering layers observed by airborne lidar. *ICES Journal of Marine Science: Journal du Conseil*, 2009.

[47] Joseph A. Shaw, James H. Churnside, James J. Wilson, Nicole E. Lerner, Rianon R. Tiensvold, Patricia E. Bigelow, and Todd M. Koel. Airborne lidar mapping of invasive lake trout in yellowstone lake. In *Proceedings of the 24th International Laser Radar Conference*, volume 11, pages 905–908, 2008.

[48] David L. Perkins and Charles C. Krueger. Dynamics of reproduction by hatchery-origin lake trout (salvelinus namaycush) at stony island reef, lake ontario. *Journal of Great Lakes Research*, 21:400–417, 1995.

[49] Sebastian J. Interlandi, Susan S. Kilham, and Edward C. Theriot. Responses of phytoplankton to varied resource availability in large lakes of the greater yellowstone ecosystem. *Limnology and Oceanography*, 44(3):668–682, 1999.

[50] Frank M. Sogandares and Edward S. Fry. Absorption spectrum (340–640 nm) of pure water. i. photothermal measurements. *Applied Optics*, 36(33):8699–8709, 1997.

[51] Curtis D. Mobley. *Light and Water: Radiative Transfer in Natural Waters*. Academic Press, San Diego, CA, 1994.

[52] André Morel. Light and marine photosynthesis: a spectral model with geochemical and climatological implications. *Progress in oceanography*, 26(3):263–306, 1991.

[53] Bonnie Kathleen Ellis. *Alternate states in a large oligotrophic lake: A retrospective analysis of nutrient loading and food web change*. PhD thesis, University of Montana, Missoula, Montana, 2007.

[54] Lusha M. Tronstad, Robert O. Hall Jr, Todd M. Koel, and Ken G. Gerow. Introduced lake trout produced a four-level trophic cascade in yellowstone lake. *Transactions of the American Fisheries Society*, 139(5):1536–1550, 2010.

[55] Joseph A. Shaw. Radiometry and the friis transmission equation. *American Journal of Physics*, 81(1):33–37, 2013.

[56] R. P. Bukata, J. H. Jerome, J. E. Bruton, and S. C. Jain. Determination of inherent optical properties of lake ontario coastal waters. *Applied Optics*, 18(23):3926–3932, 1979.

[57] Curtis D. Mobley. Polarized reflectance and transmittance properties of windblown sea surfaces. *Applied optics*, 54(15):4828–4849, 2015.

[58] Lloyd C. Bobb, Gerald Ferguson, and Michael Rankin. Laser irradiance in the sea: Theory and experiment. Technical report, DTIC, Fort Belvoir, VA, 1978.

[59] Zhong-Ping Lee, Miroslaw Darecki, Kendall L. Carder, Curtiss O. Davis, Dariusz Stramski, and W. Joseph Rhea. Diffuse attenuation coefficient of downwelling irradiance: An evaluation of remote sensing methods. *Journal of Geophysical Research: Oceans, Volume 110, Issue C2, CiteID C02017*, 110:C02017, feb 2005.

[60] Curtis D. Mobley, Bernard Gentili, Howard R. Gordon, Zhonghai Jin, George W. Kattawar, Andre Morel, Phillip Reinersman, Knut Stamnes, and Robert H. Stavn. Comparison of numerical models for computing underwater light fields. *Applied Optics*, 32(36):7484–7504, 1993.

[61] D. M. Phillips and J. T. O. Kirk. Study of the spectral variation of absorption and scattering in some australian coastal waters. *Marine and Freshwater Research*, 35(6):635–644, 1984.

[62] William Ralph Bennett. Spectra of quantized signals. *Bell System Technical Journal*, 27(3):446–472, 1948.

[63] David Sliney and Myron Wolbarsht. *Safety with Lasers and Other Optical Sources*. Springer, New York, NY, 1980.

[64] William F. Royce. Breeding habits of lake trout in new york. *Fishery Bulletin*, 52:59–76, 1951.

[65] Nigel V. Martin. Reproduction of lake trout in algonquin park, ontario. *Transactions of the American Fisheries Society*, 86(1):231–244, 1957.

[66] Stuart E. Deroche. Observations on the spawning habits and early life of lake trout. *The Progressive Fish-Culturist*, 31(2):109–113, 1969.

[67] Manu Esteve, Deborah A. McLennan, and John M. Gunn. Lake trout (salvelinus namaycush) spawning behaviour: the evolution of a new female strategy. *Environmental biology of fishes*, 83(1):69–76, 2008.

[68] A. M. Muir, C. T. Blackie, J. E. Marsden, and C. C. Krueger. Lake charr salvelinus namaycush spawning behaviour: new field observations and a review of current knowledge. *Reviews in Fish Biology and Fisheries*, 22(3):575–593, 2012.

[69] Thomas R. Binder, Henry T. Thompson, Andrew M. Muir, Stephen C. Riley, J. Ellen Marsden, Charles R. Bronte, and Charles C. Krueger. New insight into the spawning behavior of lake trout, salvelinus namaycush, from a recovering

population in the laurentian great lakes. *Environmental Biology of Fishes*, 98(1):173–181, 2015.

[70] Nathan L. Seldomridge, Joseph A. Shaw, and Kevin S. Repasky. Dual-polarization lidar using a liquid crystal variable retarder. *Optical Engineering*, 45(10):106202–106202, 2006.

[71] Charles Cox and Walter Munk. Measurement of the roughness of the sea surface from photographs of the sun's glitter. *JOSA*, 44(11):838–850, 1954.

[72] Joseph A. Shaw and James H. Churnside. Scanning-laser glint measurements of sea-surface slope statistics. *Applied optics*, 36(18):4202–4213, 1997.

[73] Rudolph W. Preisendorfer. Secchi disk science: Visual optics of natural waters. *Limnology and Oceanography*, 31(5):909–926, 1986.

[74] R. J. Davies-Colley and W. N. Vant. Estimation of optical properties of water from secchi disk depths. *Water Resources Bulletin*, 24(6):1329–1335, 1988.

[75] Michael R. Roddewig, F. Richard Hauer, James H. Churnside, Patricia E. Bigelow, and Joseph A. Shaw. Airborne lidar detection and mapping of invasive lake trout in yellowstone lake. *North American Journal of Fisheries Management*, 2017. in review.

[76] Randall M. Claramunt, Jory L. Jonas, John D. Fitzsimons, and J. Ellen Marsden. Influences of spawning habitat characteristics and interstitial predators on lake trout egg deposition and mortality. *Transactions of the American Fisheries Society*, 134(4):1048–1057, 2005.

[77] R. J. Davies-Colley and D. G. Smith. Turbidity, suspended sediment, and water clarity: a review. *Journal of the American Water Resources Association*, 37(5):1085–1101, 2001.

[78] R. Core Team. *R: A Language and Environment for Statistical Computing*. Vienna, Austria, 2016.

[79] E. Paradis, J. Claude, and K. Strimmer. Ape: analyses of phylogenetics and evolution in r language. *Bioinformatics*, 20:289–290, 2004.

[80] Roger Bivand, Tim Keitt, and Barry Rowlingson. *rgdal: Bindings for the Geospatial Data Abstraction Library*, 2016. R package version 1.2-5.

[81] Paulo J. Ribeiro Jr. and Peter J. Diggle. *geoR: Analysis of Geostatistical Data*, 2016. R package version 1.7-5.2.

[82] Martin Bachmaier and Matthias Backes. Variogram or semivariogram?: Understanding the variances in a variogram. *Precision Agriculture*, 9(3):173–175, 2008.

[83] Robert G. Wetzel. *Limnology: lake and river ecosystems.* Gulf Professional Publishing, 3rd edition, 2001.

[84] Norman Gustaf Benson. Limnology of yellowstone lake in relation to the cutthroat trout. Technical report, US Fish and Wildlife Service, 1961.

APPENDIX A

FISH LIDAR OPERATION MANUAL

Connection and Configuration Guide

This chapter describes setting up and configuring the lidar.

I have the lidar configured so it travels in two rack-mount road cases and two tupperware containers. The larger tupperware container houses the lidar head, the smaller contains the laptop and cabling.

1. Remove the lids from the larger road case which houses the laser power supply and electronics.

2. In the back of the case should be two BNC cables, one marked “interlock” and the other marked “q-switch”. Connect the cable marked “interlock” to the “remote” connector on the back of the laser power supply. Connect the cable marked ”q-switch” to the q-switch output on the back of the power supply.

3. Connect the serial cable to the RS-232 connector on the back of the power supply.

4. Run the large power cable to grid power or to where the inverter will be located. Do not power the equipment on until instructed.

5. Unpack the laser head and mount it.

6. Connect the two large gray cables to the back of the laser power supply. Note that the 4-40 jackscrews should be tightened down. Be very careful not to stress these cables too much as the jackscrews have a habit of snapping off. I have ordered spares of these parts for when the inevitable happens.

7. Connect the other ends of the cables to the laser head. Screw them down. If the cables become disconnected while the laser is on the firmware flash may be corrupted.

8. Connect two BNC cables from the gate connections on the front of the electronics rack to the gate connectors on the PMTs. These cables should be identical lengths (the cables I have purchased for the lidar are all one length so this shouldn't be an issue). These connections can be swapped from PMT to PMT, co or crosspol doesn't matter.

9. Connect two identical length BNC cables from the signal connections on the electronic rack to the appropriate PMT (these connections matter, connect the copol input to the copol PMT and vice versa).

10. Connect the power cables to the electronics rack and then to the appropriate PMT. These are the black cables with the green screw connector on one end and the PMT power connector on the other with a connector in the middle. Again, these connections matter which PMT they go to so make sure they are correct.

11. Plug the two pin connector running from the heatsink fans on the lidar head into the 12 V DC output on the electronics rack.

12. Plug an ethernet cable and 5 V power cable into the webcam on the lidar head.

13. Find and unpack the remote control box which houses the remote emergency stop, battery voltage meter, and inverter remote.

14. Plug the two pin connector for the remote emergency stop into the front panel and connect the other end to the remote control box.

15. Unpack the laptop and laptop power supply, plug the power supply into the front of the power strip in the rack. Plug the laptop in.

16. Plug the blue USB cable into the front of the electronics rack and the other end into the (blue) USB 3.0 connector on the laptop. This is a special non-standard cable so don't lose it (the only USB 3.0 bulkhead connectors I could find on Digikey required this silly cable).

17. Plug the USB GPS module into the USB connector labeled "GPS" on the front panel.

18. Connect the SMA GPS antenna to the SMA connector on the front panel (this antenna runs the GPS time server).

Inverter Connection Guide

1. Open the inverter road case and position it close to the battery. The battery cables are very short to avoid excessive voltage drop.

2. Connect the negative cable from the battery to the back of the inverter, you will need the right-angle screwdriver for this which is in the lidar toolbox.

3. Connect the positive cable which should already be attached to the inverter to the bottom of the fuse block on the battery case. Ensure it is very snug.

4. Connect the power cable from the equipment rack to the inverter. This should be the only connection that goes to the inverter. Plug other equipment into the power strip on the front of the equipment rack.

5. Connect the telephone cable to the inverter remote jack and the other end to the remote control box.

Startup Guide

1. Ensure the remote emergency stop and the emergency stop on the laser power supply are both pulled out.

2. Power the reference generator on. This is the small blue box on the left side of the electronics rack which is accessible through the slot in the front panel. The power LED should be green. If it is flashing amber unplug the USB cable and press the power button. The power LED should turn green and then you can plug the USB cable back in.

3. Power on the inverter if required.

4. Power on the lidar with the switch on the power strip.

5. Confirm that the laser power supply powers on, turn the key if necessary.

6. Test the operation of the remote emergency stop. When the emergency stop is engaged (button depressed) the yellow LED on the relay socket should go out. It should be on when the emergency stop button is pulled out. The operation can also be confirmed by checking the indicators on the laser status panel in the fish lidar application. The appropriate indicator will turn red when the emergency stop is engaged.

7. Remove the lens caps from the front of the copol and crosspol receivers. Be careful not to disturb the position of the lens tubes as this will rotate the polarizer.

8. At this point the lidar is ready to operate.

Software Guide

Usage Guide

The lidar software is located in `C:\fish-lidar\`.

1. Start the software.

2. In the small dialog window that opens select an appropriate campaign file or create a new one.

3. Select the calibration file if you want the software to display received data in radiance instead of digital number (this does not affect how the software writes values into the campaign database, this is always written as digital number). Also make sure the "Use Calibration?" box is checked if you want to use the calibration file.

4. Confirm the other settings are correct. Typically the laser and GPS serial adapters come up as the same COM ports so these settings should not need to be modified. Delay generator should be set to CmodS6 unless for some reason it is not present. Tilt angle is for the tilt of the lidar head in degrees. Remarks are any notes you wish to record in the database for this run.

5. Click "done".

6. The software should boot the hardware and the laser should go from sleep to standby mode. Note that it will take some time for the laser to warm up at this point, you can ask the software to start collecting but the laser will not fire until it is warmed up. The laser will indicate it is in a warning and/or not ready state until it is at the correct temperature.

7. At this point the software is ready to collect data. Collection can be started and stopped as needed with the "Start Collection" button. Confirm that the laser shutter is open.

8. Sometimes (often) one of the digitizers will hang. Stop collection and shut down the software and open the "cstest64" program from the Start Menu. Select the offending digitizer (unless you switched them in the lidar application the copol

digitizer will be the first digitizer listed, crosspol second). Go to the controls menu and do a system reset. The cstest64 program will crash, this is quality software we're dealing with here. Usually this will fix the hung digitizer but sometimes it will continue to hang. Continue resetting it with the cstest64 application until it functions. Happily once it is running it will continue to run until a power cycle, so don't despair too much.

General Notes

- To switch campaign files you must restart the program. There is currently no facility to do this once the program has been started.

- The laser status is no longer printed to the console. However, the documentation on the interlock status byte is not correct. I was able to deduce which flags indicated the front-panel emergency stop and the remote emergency stop but I have no way of knowing what the other bits are. I assume they are as indicated in the laser documentation but this may not be correct. In any case in the event of an interlock condition the top "Interlock" indicator will still illuminate as the global byte documentation is correct.

- If one channel or the other saturates a "[channel] saturated" warning will illuminate on the top plot. The exact point at when a channel is considered to be saturating can be adjusted in the `Fish Lidar.exe.config` file. `SaturateLevel` changes the (absolute) level at which a point is considered to be saturating. The units are in digital number from the digitizer. `SaturatePoints` is the number of points which need to be above the `SaturateLevel` before the saturation warning will illuminate. The defaults are 8191 and 50, respectively.

- The TimeMachines TM-1000A is an NTP time server synchronized to GPS time. This is the master time source for the instrument and the laptop and camera (and all other devices that are connected via ethernet) should be synchronized to this time server. At the time of writing it is at 192.168.1.15, and the admin password is "tmachines". The details of how to configure each device to use the time server are beyond the scope of this manual, but instructions are readily available over the internet.

Compilation Guide

The software repository contains all the pieces needed to compile the software out of the box. Open the project in Visual Studio 2015, set the appropriate output directory and hit compile.

The API documentation is generated using Doxygen. Install Doxygen on your computer and open the Doxyfile in the doc directory in the wizard. Make sure the configuration file has the appropriate directories set and then run Doxygen.

Software Design Description

The software is designed to be modular, each piece performs only one function to make it easy to understand and maintain. The Doxygen-generated documentation is the best description of the software.

Several threads run in the software. One is located in the `Database` class and handles all writes to the database. Another is in the `Lidar` class and processes the lidar data. Each digitizer has its own thread that checks for digitizer data and sends this data to the lidar class for processing. Another thread runs in the `Laser` class and handles all communication with the laser. These threads must be stopped before closing the software.

Database Schema

The `lidar` table contains the captured data. The returns from each channel are stored at 16-bit signed integer arrays. A timestamp is generated when the data is first received from the digitizers. Due to USB latency this may not be the exact time the data was first captured. This timestamp is stored as a Julian day number which may be converted back to a text date and time by using the function in SQLite. For each row there is also an ID of the calibration that was associated with that capture, if one was provided when the program was started, and an ID of the specific lidar configuration which stores the head tilt, sample rate, and any associated remarks.

The contents of the other tables are self-explanatory.

System Description

The lidar consists of three main components: the laser and supporting hardware, the optical assembly and PMT receivers, and the digitizers.

Laser

The laser is a Big Sky Laser (now Quantel) Centurion with a frequency doubler to convert the 1064 nm output to 532 nm. The head is mounted on one side of the optical breadboard. Output polarization is perpendicular to the base of the laser. The laser is connected to the power supply with two d-sub cables, one of which provides power and the other which carries data signals. These connections need to be tight, if they are loose the laser may not function. The q-switch output from the laser is used to trigger the PMT gates.

Receivers

The optical assembly is mounted on an aluminum rail so that it can be adjusted to align the optics. The aperture stop (iris) is also adjustable in X and Y and is adjusted by transmitting a collimated beam into the optics and adjusting the iris for maximum power output. This should be done on an optical bench before rough adjustment of the assembly on the rail.

The PMTs have three connections: power, signal, and gate. The gate signal is used to turn the PMTs on and off and is driven by the q-switch output from the laser power supply (presumably through a timer of some sort but I've never seen a schematic for the electronics board). The power signal supplies the +15 V supply power and the gain voltage to the PMTs. The gain voltage varies between +2 and +5 V and is sourced by the Phidget DAC card. The lidar software has an option to specify which channel of the DAC is hooked to which PMT or you can swap the signals using the connectors that are on the electronics rack. The signal outputs are hooked directly to the digitizers (do not run them through the electronics board as the electronics board was not designed in an RF friendly way).

Because the digitizers run at 800 MSPS it is important to treat the signal lines from the PMTs as RF connections (controlled impedance and shielded). Do not coil the signal lines and try to avoid routing them close to any noise sources.

In the future it would probably be wise to put an anti-alias filter and some sort of AGC in front of the digitizers.

Each of the receivers has a polarizer that is RTVed to the lens mount and then fastened down with the retaining ring. The co-polarizer is 1 degree off from vertical, the cross-polarizer is 4 degrees off from horizontal. The polarizers were laser cut from a piece of Edmund Optics 45-668 polarizer sheet.

PMT Power Supply Filter

At one point I noted that the recieved signal had a persistent noise blip. Through investigation I found that the 15 V supply line had 2 V_{pp} ripple present. I designed a filter board to remove this ripple and installed it in the electronics rack.

Software Utilities

In the fish-lidar-utility repository are several scripts for performing various tasks with the lidar and lidar data.

fishdataprocessory.py (processes raw campaign databases)

The purpose of the data processor is to process a raw campaign database into a processed database which can then be analyzed using other utilities. Briefly it computes the location of each shot, converts the digitizer output into radiance, performs surface detection for each shot, and also corrects for some bugs that were present in older versions of the lidar application software. Comprehensive documentation on the data processor is available through `fishdataprocessor.py --help`, however, the default options should be sufficient for most flights.

fishimages.py (creates images from a processed lidar database)

`fishimages.py` creates images of the lidar data from a processed lidar database. Most commonly I run this utility using a "job file" which sets options specific to each lake, including the creation of appropriate output directories. The utility can then be invoked through a BASH for loop on multiple databases and stores all the images in the appropriate directory, which saves me a ton of time. There is currently no documentation on the job file format, however, the options are the same options if the image utility is not invoked in job mode. The best documentation is to read one

of the sample job files (`yellowstone.cfg` or `flathead.cfg`). 16-bit mode currently does not work and was only partly implemented. I found that producing false-color images provided sufficient dynamic range. One advantage of completing the 16-bit implementation is the image can then be geo-referenced.

fishatten.py (calculates attenuation coefficients from a processed lidar database)

This utility produces a CSV file of lat/long and calculated lidar attenuation coefficient for each shot. The options are self-explanatory.

fish-lidar-utilities (various utility functions in one directory

)

`dbslice.py` Extracts a portion of a processed database.

`flatheadfix.py` Old software that was used to correct an issue with a specific flight.

`gpsextract.py` Extracts GPS data from images from the 2004 flight with the NOAA lidar.

`kmlexport.py` Exports a KML file of the flight path from a processed fish lidar database.

`locater.py` Probably the most useful utility, determines the lidar position from a timestamp. Used in locating fish and other items of interest seen in the lidar data.

`modifycal.py` Will replace the calibration in a database with the one provided.

`spatialtomat.py` Records data from the Phidgets Spatial into a MAT file. Used for testing.

fishcalibrate.py (calibration utility)

The lidar software is designed to handle a calibration in radiance with the PMT gain voltage and PMT output being the input parameters. The polynomial is

$$L_e = p_{00} + p_{10} \cdot g + p_{01} \cdot y + p_{20} \cdot g^2 + p_{11} \cdot gy + p_{30} \cdot g^3 + p_{21} \cdot g^2 y + p_{40} \cdot g^4 + p_{31} \cdot g^3 y \quad \text{(A.1)}$$

where L_e is radiance measured in W/cm^2/sr/nm, g is PMT gain in volts, and y is the PMT output in volts.

The calibration utility is named `fishcalibrate.py`. It requires PyVISA, SciPy, NumPy, and the Phidgets driver to function. The utility was written to function with a Tektronix TDS3054B connected to the computer via ethernet. The PMT output signal is expected on channel 1 and the PMT gate signal on channel 2. It may also be necessary to edit the DAC channel mapping. This is changed by editing the program itself and changing the copol and crosspol variables.

The only hardware that is necessary for calibration is the telescope receiver being calibrated, the integrating sphere, the DAC to set the PMT gain voltages, and the oscilloscope. To perform a better calibration the oscilloscope should be replaced with the digitizer for the channel in question, but that has not yet been implemented.

It is assumed that the telescope will be pointing in to the integrating sphere (at the time of writing it lives in Unit 21), and the computer will be hooked to the ammeter and the integrating sphere attenuator.Connect the integrating sphere attenuator to the computer and note which port it is on. Connect the GPIB adapter to the computer so the software can talk to the ammeter. Connect a signal generator to the gate input of the PMT, set to 50 us pulse width, 0 V low value, 4 V high value, 1 kHz frequency, 5 ns edge width. Connect the sync output of the signal generator

(ensure it is enabled) to channel 2 of the oscilloscope. Connect the PMT signal output to channel 1 of the oscilloscope.

The utility contains a terminal which is used to perform the calibration. Help can be accessed in the software by typing "help". In essence the procedure is to set the run settings for the calibration run in the terminal and then run the calibration. The default settings are designed to be sufficient for most cases.

The MAT file that is saved from the utility contains three arrays, one of the input radiances, another of the input gains, and a third of the outputs. This file can be imported into MATLAB and a curve fit on a 4x1 polynomial performed using `fit` or other software. The polynomial coefficients are then entered into an INI file, an example of which is given in the software repository as `cal20140606.ini`. The `MinGain` and `MaxGain` parameters indicate the minimum and maximum gains over which the fit was performed. I noted while performing the first calibration that the PMT response below a gain of voltage of 3.5 V was very non-linear, so did not calibrate below that point. The numeric data can be entered in any format that will be understood by the C# `Convert.ToDouble(string)` method.

fishexport.py (data export to HDF5 utility)

This utility exports data from a campaign database to an HDF5 file for import into MATLAB. Help can be obtained by typing `fishexport.py --help`.

Pre-Flight Checklist

☐ Lens covers removed.

☐ Laser shutter opened.

☐ Waveplate installed/not installed and correct polarizers installed for experiment.

☐ Presence/absence of diverging lens for experiment.

☐ Correct receiver telescopes installed for experiment.

☐ Polarizers aligned correctly.

☐ Power on the 10 MHz reference generator.

☐ Power on lidar.

☐ Verify digitizer fan tray power on.

☐ Verify correct operation of remote emergency stop.

☐ Zero gyro.

Pre-Collection Checklist

☐ GPS locked.

☐ GPS atomic clock locked.

☐ Filename correct.

☐ Calibration file correct.

☐ Computer date/time accurate and synchronized to GPS time.

☐ Video date/time accurate and synchronized to GPS time.

☐ Video recording on.

Packing Checklist

Components

- ☐ Lidar head
- ☐ Electronics rack
- ☐ Inverter rack
- ☐ Battery
- ☐ Remote emergency stop
- ☐ USB GPS module
- ☐ Non-standard USB 3.0 cable for computer
- ☐ USB 2.0 extension cable
- ☐ Fish lidar laptop
- ☐ Laptop charger
- ☐ (2) matched BNC cables for PMT gate connection
- ☐ (2) matched BNC cables for PMT signal connection
- ☐ (2) PMT power cables
- ☐ Tie-down straps
- ☐ Wide FOV diverging lens and mount
- ☐ Wide FOV receivers
- ☐ Wide FOV apertures

Spares

- ☐ Spare battery fuses
- ☐ Spare jackscrews for laser power supply
- ☐ Spare jacknuts for laser power supply

Tools

- ☐ Phillips head screwdriver
- ☐ Flathead screwdriver
- ☐ Right angle flathead screwdriver
- ☐ Adjustable wrench
- ☐ Allen wrench set
- ☐ Zip ties
- ☐ Flush cutters
- ☐ Electrical tape
- ☐ Oscilloscope
- ☐ Protractor
- ☐ 1” optics wrench
- ☐ 5/32 hex wrench